Department of Construction Sciences
Solid Mechanics

ISRN LUTFD2/TFHF-18/5226-SE(1-93)

Modeling of pillow-shaped paperboard packages subjected to compression

Master's Dissertation by

Pontus Thuresson

Supervisors:
Professor Matti Ristinmaa, Div. of Solid Mechanics
Ph.D. Anders Magnusson, Tetra Pak Packaging Solutions AB

Examiner:
Professor Mathias Wallin, Div. of Solid Mechanics

Printed by Media-Tryck AB, Lund, Sweden
For information, address:
Division of Solid Mechanics, Lund University, Box 118, SE-221 00 Lund, Sweden
Webpage: www.solid.lth.se

Abstract

This thesis treats compression testing of pillow-shaped paperboard packages. The packages, called Tetra Fino® Aseptic, are a part of the Tetra Pak package portfolio. Virtual packages were defined and compression tests, simulated using the commercial software Abaqus, were compared to physical compression tests of actual packages.

The tests were conducted using different package configurations. Initially a single package was tested both physically, obtaining force-displacement data, as well as virtually, obtaining stresses, strains and pressure data. Then two packages were used in order to test different package overlaps. Different number of package layers were tested virtually as well. Also in these cases, output was obtained in form of force-displacement data, stresses, strains and pressure data.

It was concluded that it is only partially possible to compare virtual and physical data directly by means of the methods in this thesis. The overall behaviour of a package may be estimated, but actual stress and strain states may not.

Of the three overlaps tested, 12.5%, 25% and 50%, it was concluded, both by testing and by simulations that 12.5% overlap is the best in terms of resisting compressive loads. From simulations, it was also shown that stacking two or three packages on top of each other has no effects on the build-up of internal pressure of the package.

Keywords: pillow-shaped package, FEM, compression testing, packing patterns

Acknowledgements

The work of this Master's thesis was conducted at the Lund office of Tetra Pak from January to June 2018. It was conducted as a final examination for the mechanical engineering programme at Lund University, on the behalf of the Division of Solid Mechanics.

First and foremost, I would like to thank my supervisor Anders Magnusson who I have always been able to discuss issues and concerns with. He has provided me with helpful ideas and vital insights. This thesis could not have been done without him. I would also like to thank the rest of the members of the advanced virtual engineering group at Tetra Pak; Paul Håkansson, Daniel Vojskovic and Lotta Bergstrand, who have provided me with reflections and feedback on my work. Especially Lotta has been particularly involved in my work, helping me throughout the entire process.

Furthermore, I would like to thank Claes Wallin-Klevås for sharing his knowledge and experience with package-related questions and Emma Fors for all her assist with the compression tester. I also express my gratitude towards all other employees at Tetra Pak who made this thesis possible.

Even though most of the work has been conducted at Tetra Pak, I would still like to thank my supervisor Matti Ristinmaa for his comments and thoughts on the work, and for his help structuring and finalizing it.

Finally, I would like to thank my family for all their support.

Lund, June 2018

Pontus Thuresson

Contents

CHAPTER 1

Introduction

1.1 Background

This Master's thesis treats the Tetra Fino® Aseptic, which is a package within the package portfolio of Tetra Pak. The Tetra Fino® Aseptic is manufactured in the Tetra Pak® A1 filling machine where it is formed to a pillow shape. It is made from a plastic laminated cardboard material including aluminium foil. It mainly holds liquid dairy products such as milk or juices, even though it may also contain e.g. ice cream.

Tetra Fino® Aseptic is mainly present in developing countries where the conditions during packing, distribution and storing are challenging. The challenging conditions sometimes damage the packages and require Tetra Pak to recommend secondary packaging solutions to be able to cope with these conditions in the best way.

Tetra Pak recommends different packing patterns for Tetra Fino® Aseptic packages. Boxes with different packing patterns have different performances during transportation. Customers are recommended to choose a secondary box/packing height so that the primary packages take no load. However, in reality there are many cases where this is not the case and the primary pack still have to take some load. For this reason it is relevant to improve knowledge of how various Tetra Fino® Aseptic packing patterns will respond to compressive loads.

1.2 Package information

The Tetra Fino® Aseptic package is formed by closing the ends of a paperboard tube. There are folds and wrinkles appearing due to the forming process, where some wrinkles are predicted and others appear somewhat randomly. A Tetra Fino® Aseptic package is shown in Figure 1.1.

Figure 1.1: Tetra Fino® Aseptic package [9].

The material used for the packages at Tetra Pak is a multiply laminate. It consists of six plies, of which one ply is paperboard, one ply aluminium and four plies are polyethylene. The composition may be seen in Figure 1.2. The purpose of the layers of polyethylene on the package inside and outside is to prevent moisture from entering or exiting the package. The interior layers of polyethyle are used as cohesive layers, in order to bind the paperboard and aluminium. The paperboard gives structure to the package and the aluminium is used as a barrier for light and oxygen [8].

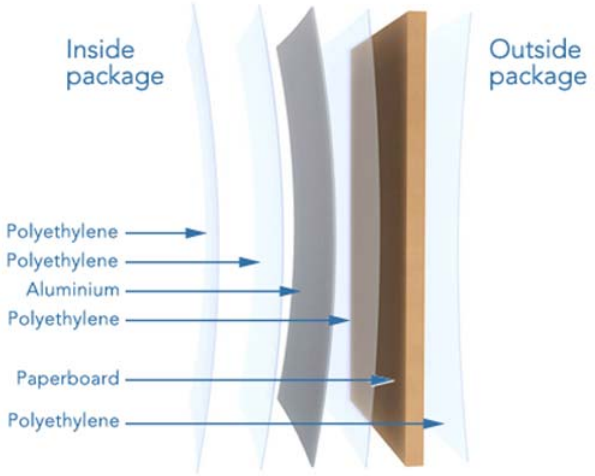

Figure 1.2: Multiply laminate package material used at Tetra Pak [8].

A package nomenclature is commonly used at Tetra Pak in order to make referencing simpler. The transversal seal of the Tetra Fino® Aseptic package is normally abbreviated as TS, whereas the longitudinal seal is abbreviated LS. When referring to different locations on the package, the terms frontside, backside, top and bottom are used. The positions are defined from a package being held with the primary print facing forwards and having the correct orientation of the print. Both TS and LS as well as the orientation of the package is shown in Figure 1.3.

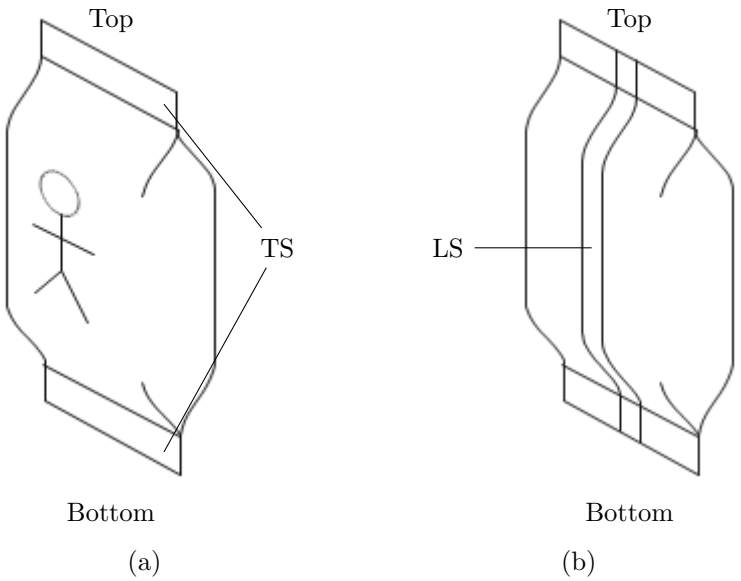

Figure 1.3: Terminology for Tetra Fino® Aseptic packages. a) Frontside b) Backside.

When it comes to packing patterns of the packages, and particularly stacking of packages, the term *overlap* is used. There are two types of overlaps - shortside (OLS) and longside (OLL). A shortside overlap will have the TS overlapping, whereas a longside overlap has the packages overlapping in their width direction. The overlap indicates how much of the bottom package that is covered by the top package. If it is completely covered, a 100 % overlap is used. A schematic picture of two packages, with the shortside overlap depicted, is shown in Figure 1.4. Packages placed in patterns without any overlap is normally denoted column packing (COL).

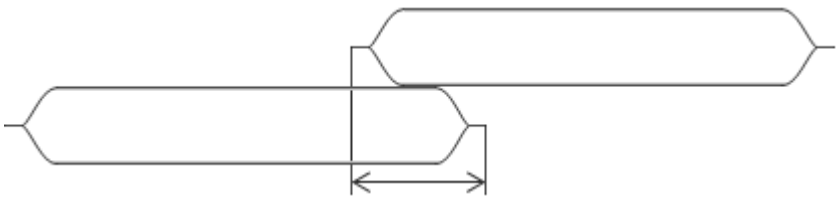

Figure 1.4: Definition of shortside overlap. It may be measured either in a length unit or by a percentage of the package length.

1.3 Package fracture behaviour

Previous compression tests of Tetra Fino® Aseptic packages conducted by Tetra Pak show that packages will rupture, not in the seal (TS), but in a close perimeter to the seal. This has also been shown virtually, not in a compression test but in a wedge test. In a wedge test, two material strips are sealed together and then pulled over a wedge shaped metal plate until the strips break. The principle of a wedge test is shown in Figure 1.5. In this case, the material strip is deformed very similarly to the edges of a package in a compression test. Due to this fact, it is reasonable to assume that the fracture behaviours of a wedge and compression test are similar as well.

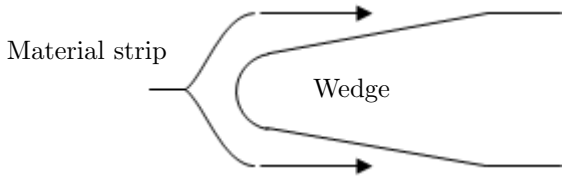

Figure 1.5: Principle of wedge testing. A material strip is dragged over a wedge shaped plate rounded at the front.

Figure 1.6 shows a simulation of a wedge test conducted by Tetra Pak. As seen, the seal will be intact, whereas the material in a close perimeter to the seal will be critically loaded. The inner layer, the aluminium foil and the adhesive will delaminate from the rest of the package material. Also the paperboard will show some self-delamination. Due to the delamination, the local load will be taken almost entirely by the aluminium, since the polymers are ductile and show very little structural integrity. Necking of both the polymers and the aluminium foil may be noticed, localized to a small zone close to the seal. This should mean that stresses and strains are locally high, whereas the rest of the packaging material show a more uniform distribution. Due to the fact that the aluminium foil is much more brittle than the polymers, this layer will most likely be the first to fracture. Once the structural integrity is lost, the polymers will elongate unhindered and eventually break as well. From that point, there are two possibilities. Either the paperboard will hold some further loads until it breaks, or the fluid contained in the package will soak the paperboard and exit through the end of the seal.

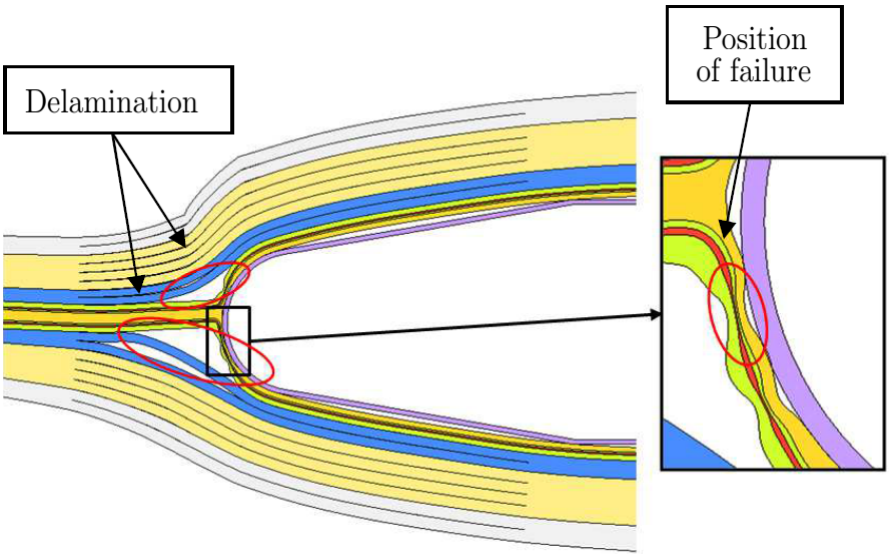

Figure 1.6: Predicted fracture behaviour of packaging material from a wedge test simulation [7].

1.4 Previous testing of packing patterns

Tests showing variations in robustness of Tetra Fino® Aseptic packing patterns have previously been conducted at Tetra Pak. In these tests, packages were placed in cardboard boxes in the same way as they would be if they were to be transported. The patterns that were used for the testing were column patterns, OLS patterns and OLL patterns (c.f. Section 1.2). In a layer, either 2x2 or 2x3 packages were packed, and the number of layers was either 3 or 4. In this particular case, 30 tests of each pattern were conducted. The results of these tests are shown in Figure 1.7.

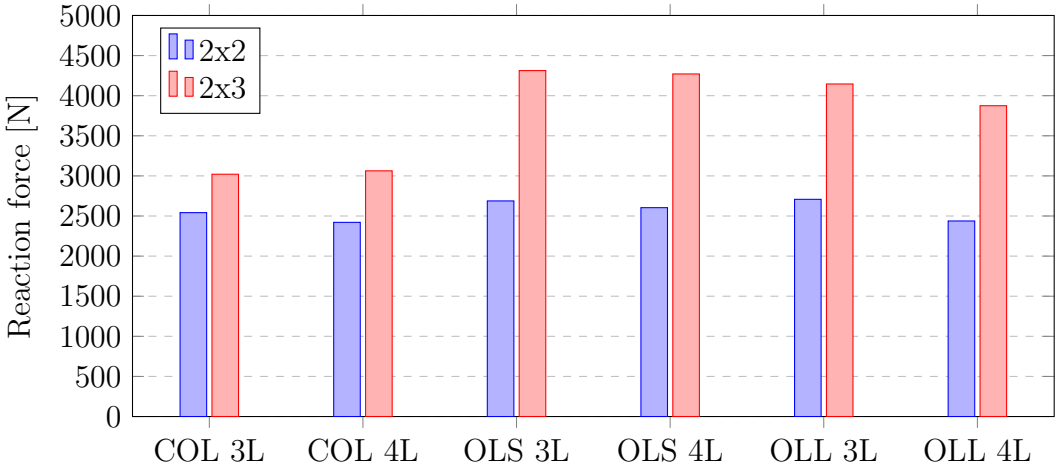

Figure 1.7: Results from compression tests of different packing patterns conducted at Tetra Pak. Column (COL), OLS and OLL patterns with either 3 (3L) or 4 (4L) layers were used in the testing [7].

From the figure, it may be seen that there is an indication of that shortside overlap (OLS) is slightly more robust than both the column (COL) and longside overlaps (OLL). It may also be seen that, in general, three layers (3L) tend to be more robust than four layers (4L) for the same pattern.

1.5 Aim and problem formulation

The aim of this master thesis is to subject Tetra Fino® Aseptic packages to static compressive loads in order to study what factors that may affect the robustness of the package. By robustness is meant the ability to withstand damage of the package in form of material tears.

At first hand, single packages should be tested physically in order to find whether it is possible to replicate the behaviour of a Tetra Fino® Aseptic package by a virtual model. It should be investigated whether it is possible to find an indicator, or criterion, that may indicate imminent fracture of the package.

Secondly, both physical and virtual tests should be conducted on multiple packages as well. More specifically, various packing patterns of the Tetra Fino® Aseptic packages should be investigated, in order to find which factors that may affect robustness.

1.6 Limitations

When it comes to modeling of the package material, it is limited to be a macroscopic continuum model, which does not take the microstructure of the material into consideration. With reference to previous data in Section 1.4 this thesis will primarily look at patterns with shortside overlaps.

CHAPTER 2

Theory

In this chapter, the theory necessary for understanding various models used to describe different physical phenomena is presented. The main focus is the modeling of materials and their behaviour in elasticity, yielding and plasticity. Also the finite element discretization method with corresponding solution methods is presented.

2.1 Large deformations

Consider an arbitrary body in some coordinate system. The coordinates of a material point in the body are initially given by $x_i^0 = (x_1^0, x_2^0, x_3^0)$. If the body is deformed, this point will move in space and acquire a new set of coordinates $x_i = (x_1, x_2, x_3)$. Hence, there is both an undeformed and a deformed configuration for this material point. Next, consider a line element dx_i^0 in the undeformed configuration. In the deformed configuration this element is instead denoted dx_i. The deformation of the element is obtained from the differential $dx_i = F_{ij}dx_j^0$. Here, the deformation gradient $F_{ij} = \dfrac{\partial x_i}{\partial x_j^0}$ is introduced for simplicity. The determinant of the deformation gradient is normally called the *Jacobian* $J = \det(F_{ij})$.

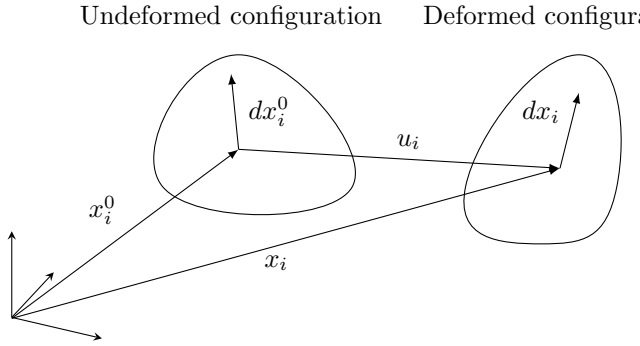

Figure 2.1: Deformation of an arbitrary body [4].

The deformation may also be expressed using the displacement u_i, in the following manner $x_i = x_i^0 + u_i \Rightarrow dx_i = d(x_i^0 + u_i) = \frac{\partial x_i^0}{\partial x_j^0} dx_j^0 + \frac{\partial u_i}{\partial x_j^0} dx_j^0 = (\delta_{ij} + u_{i,j}) dx_j^0$. It may thus be noted that $F_{ij} = \delta_{ij} + u_{i,j}$ [4].

2.1.1 Strain measures

The strain of a line element may be measured in various ways. In this case, use is made of the logarithmic strain, which in the uniaxial case is defined as

$$\varepsilon^l = \ln(\frac{dl}{dl^0}) \tag{2.1}$$

where dl is the deformed length and dl^0 the undeformed length of the line element. The ratio dl/dl^0 is called the *stretch* and is denoted Λ. With reference to the previous section, $dl = \sqrt{dx_i dx_i}$ and $dl^0 = \sqrt{dx_i^0 dx_i^0}$, which means that

$$\Lambda = \frac{dl}{dl^0} = \frac{\sqrt{dx_i dx_i}}{\sqrt{dx_k^0 dx_k^0}} = \frac{\sqrt{F_{ij} dx_j^0 F_{il} dx_l^0}}{\sqrt{dx_k^0 dx_k^0}} = \sqrt{F_{ij} n_j F_{il} n_l}$$

if the following unit vectors are introduced

$$n_j = \frac{dx_j^0}{\sqrt{dx_k^0 dx_k^0}} \qquad n_l = \frac{dx_l^0}{\sqrt{dx_k^0 dx_k^0}}$$

Furthermore, by using the so-called polar decomposition theorem, the deformation gradient may be decomposed into a rotational and a stretching part as $F_{ij} = R_{ik}\Lambda_{kj}$,

where R_{ik} is the rotational tensor and Λ_{kj} the *stretch tensor* [4]. By decomposing the deformation gradient in the expression of the stretch, the following is obtained

$$\Lambda = \sqrt{R_{ik}\Lambda_{kj}n_j R_{im}\Lambda_{ml}n_l}$$

A specific property of the rotational tensor R_{ik} is that it is orthogonal, i.e. $R_{ik}R_{im} = \delta_{km}$, which means that the stretch may be rewritten further as

$$\Lambda = \sqrt{\delta_{km}\Lambda_{kj}n_j\Lambda_{ml}n_l} = \sqrt{\Lambda_{mj}n_j\Lambda_{ml}n_l}$$

In conclusion, a relation between the stretch and the stretch tensor, i.e. between the uniaxial and three-dimensional case, has been found. The interpretation of the expression is, in broad terms, that the stretch is obtained by projecting the stretch tensor onto the normal vector in the direction of the stretch.

The logarithmic strain tensor ε^l_{ij} may now be introduced symbolically as $\varepsilon^l_{ij} = \ln(\Lambda_{ij})$, in analogy with Equation (2.1). Other possible choices are the Green's strain tensor $\varepsilon^G_{ij} = \frac{1}{2}(F_{ki}F_{kj} - \delta_{ij})$ or the right Cauchy-Green deformation tensor $C_{ij} = F_{ki}F_{kj}$. The choice will here be put on logarithmic strains since they are suitable for large strain and large deformation loading situations [1]. The l index of the strains will be omitted for simplicity, hence stating the strains as ε_{ij} [4].

2.1.2 Stress measures

The traction vector t_i is introduced as the incremental force dF_i divided by the incremental area dA on which it is acting, when the area approaches zero, i.e.

$$t_i = \lim_{dA \to 0} \frac{dF_i}{dA}$$

The area may be taken at some internal section or external surface of an arbitrary body. The surface normal of dA is denoted n_i. A visualization of the introduced quantities may be seen in Figure 2.2 a).

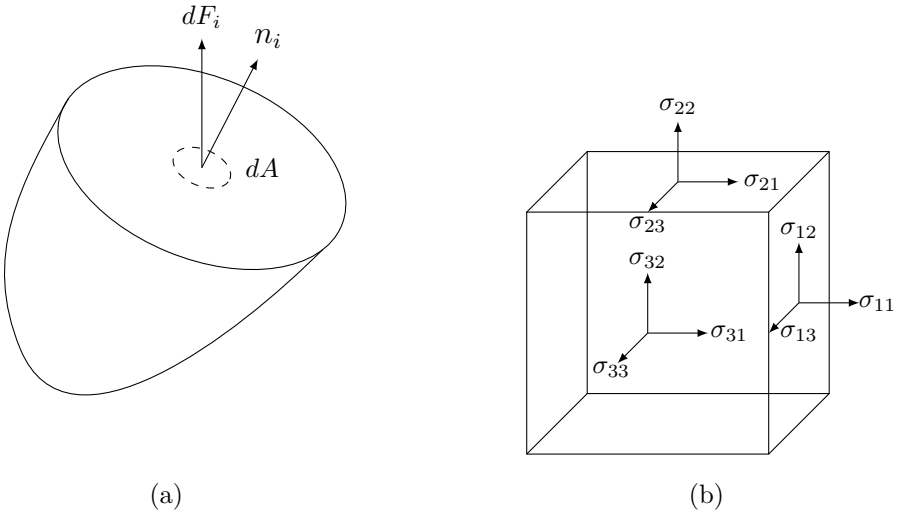

Figure 2.2: a) Definition of the traction vector acting on an arbitrary body. b) Stress components of the stress tensor acting on orthogonal planes of an infinitesimal volume element.

The area dA may be chosen depending on which configuration, whether it is the reference or deformed, that is used. In this case, Cauchy stress, or true stress σ is used which means that the reference area dA is chosen from the deformed configuration. If instead the reference area is taken as the undeformed area the first Piola-Kirchhoff stress is obtained. Multiplying the first Piola-Kirchhoff stress tensor by the deformation gradient provides the second Piola-Kirchhoff stress tensor.

Next, consider an infinitesimal volume element, with three principal planes in space. If the traction vector is divided into components, two in-plane and one orthogonal to each principal plane, a total of nine components may be introduced. These are denoted *stress components* and may be seen in Figure 2.2 b). The stress components may then be gathered by introducing the *stress tensor* σ_{ij}, where e.g. the component σ_{11} may be found as component 11 of the tensor. A property of the stress tensor is that it is symmetric, i.e. $\sigma_{ij} = \sigma_{ji}$. The proof if this is found by using the momentum equations. However, it is omitted in this text [4].

Finally, the relation between the traction vector and the stress tensor may be expressed as $t_i = \sigma_{ij} n_j$, in accordance with Cauchy's principle [6]. Here, n_j is the surface normal of an arbitrary surface, as introduced earlier.

2.2 Material symmetries

The most general type of materials are known as *anisotropic materials*. On the other hand, materials which are independent on load direction, i.e. where every plane is a

symmetry plane are called *isotropic*. In between these extremes, there may be various material configurations and a particular type is orthotropic materials. These materials have properties that are direction dependent, with three symmetry planes about which the material properties are mirrored. Various material configurations may be seen in Figure 2.3.

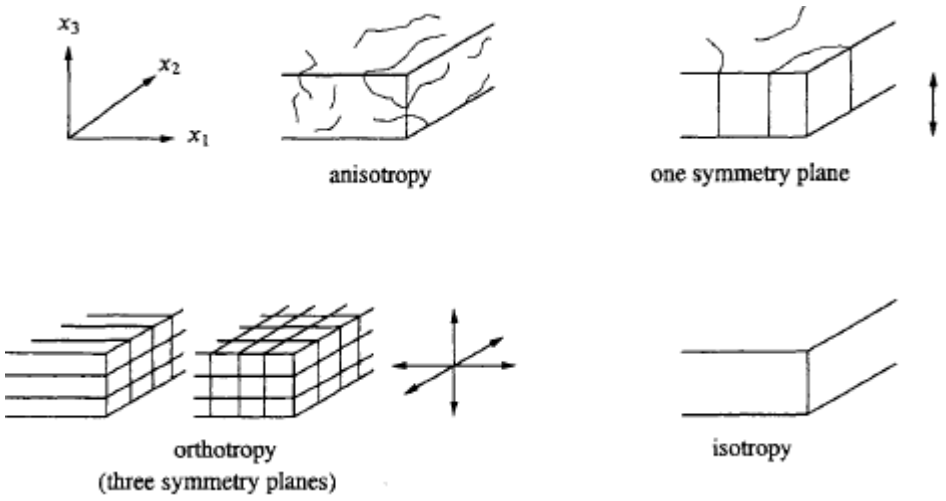

Figure 2.3: Different levels of material symmetry. Anisotropic materials have zero symmetry planes, orthotropic materials have three and for isotropic materials, every plane is a symmetry plane [5].

2.3 Hyperelasticity

A general elastic material where the stresses have a unique relation to the strains is called a Cauchy material. A special type of Cauchy material, where the stress/strain relationship is derived from a potential function in form of the strain energy W, is called a *hyperelastic* material. By using the unique stress/strain relation $\sigma = \sigma(\varepsilon)$, assuming second Piola-Kirchhoff stresses and Green's strains, the strain energy W of a material in the uniaxial case may be expressed as

$$W = \int_0^{\varepsilon} \sigma(\varepsilon) d\varepsilon \tag{2.2}$$

This is shown in Figure 2.4. Assuming the strain energy to be independent of load history, it is hereby shown that the strain energy is function of strains alone. From Equation (2.2), it is evident that $dW = \sigma_{ij} d\varepsilon_{ij}$, since $W = \int dW$. On the other hand, since the strain energy is solely a function of strains, $W = W(\varepsilon_{ij})$, the incremental strain may also be expressed as

$$dW = \frac{\partial W}{\partial \varepsilon_{ij}} d\varepsilon_{ij}$$

Hence, the conclusion is that

$$\sigma_{ij} = \frac{\partial W}{\partial \varepsilon_{ij}} \tag{2.3}$$

i.e. the stresses are derived from the strain energy, which serves as a potential function. The constitutive relation between stresses and strains for hyperelastic materials has thereby been found [5].

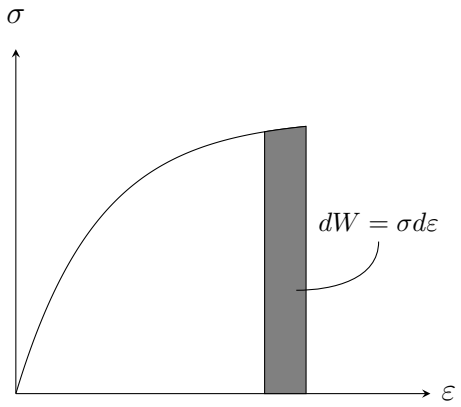

Figure 2.4: Strain energy found from integration of the stress [5].

2.3.1 Arruda-Boyce form

One type of hyperelastic material is the Arruda-Boyce form. The strain energy of this type of material is given by the expression in Equation (2.4) [2] [1],

$$W = \mu \sum_{i=1}^{5} \frac{C_i}{\lambda_m^{2i-2}} (\tilde{L}_1^i - 3^i) + \frac{1}{D} \left(\frac{J_{el} - 1}{2} - \ln J_{el} \right) \tag{2.4}$$

Here, μ is the shear modulus, λ_m the so-called locking stretch, $\tilde{L}_1$ the first deviatoric stretch invariant, D a compressibility ratio proportional to the inverse of the bulk modulus, J_{el} the elastic Jacobian (or volumetric strain). The compressibility ratio is defined as $D = 2/K_0$, where K_0 is the initial bulk modulus. The shear modulus has the following relation to the initial shear modulus

$$\mu_0 = \mu \left(1 + \frac{3}{5\lambda_m^2} + \frac{99}{175\lambda_m^4} + \frac{513}{875\lambda_m^6} + \frac{42039}{67375\lambda_m^8} \right)$$

The locking stretch is the ratio between a fully stretched polymer chain and the corresponding unstretched chain. The first deviatoric stretch invariant is defined as the quadratic sum of the principal deviatoric stretches $\tilde{L}_1 = J^{-\frac{2}{3}}(\Lambda_1^2 + \Lambda_2^2 + \Lambda_3^2)$ where J is the Jacobian. J_{el} is defined as the ratio between the total volume change and volume change due to thermal effects, $J_{el} = J/J_{th}$. C_i are constants given by

$$C_1 = \frac{1}{2} \quad C_2 = \frac{1}{20} \quad C_3 = \frac{11}{1050} \quad C_4 = \frac{19}{7000} \quad C_5 = \frac{519}{673750}$$

The stress tensor is then determined by (2.3).

2.4 Yield criteria

As an indication of initiating plasticity a *yield criterion* may be used. The yield criterion is fulfilled when the so called *yield function* f is zero. After exceeding the elastic region of a material, plasticity is initiated. The load at which this occurs is called the *initial yield stress*, σ_{y0}. If the material is unloaded at this point, it will be elastically unloaded, i.e. no permanent deformations are obtained. If the load is increased, however, plastic strains, ε_{ij}^p, are introduced. These are only changed if the material is yielding, so for every plastic strain state, there must also be a corresponding yield stress called the *current yield stress* σ_y.

For isotropic materials, it is common to use the von Mises yield criterion, which may be expressed as $f = \sigma_{eff} - \sigma_y = 0$, where σ_{eff} is the Mises effective stress, defined as

$$\sigma_{eff} = \sqrt{\frac{3}{2} s_{ij} s_{ij}}$$

The effective stress is defined using the *deviatoric stress tensor* $s_{ij} = \sigma_{ij} - \frac{1}{3}\sigma_{kk}$. In principal stress space, the von Mises yield function represents a circle in the deviatoric stress plane, as shown in Figure 2.5.

For orthotropic materials, Hill's yield criterion may instead be used. It has six independent parameters F, .., N which have to be determined experimentally, and it takes the following form

$$F(s_{11} - s_{22})^2 + G(s_{11} - s_{33})^2 + H(s_{22} - s_{33})^2 + 2Ls_{12}^2 + 2Ms_{13}^2 + 2Ns_{23}^2 - 1 = 0 \quad (2.5)$$

Here, s_{ij} correspond to deviatoric stress tensor components. Morover, the parameters F, G and H are related to the yield stresses in each principal direction, σ_{y0}^{11}, σ_{y0}^{22} and σ_{y0}^{33} according to

$$F = \frac{1}{2}\left[\frac{1}{(\sigma_{y0}^{11})^2} + \frac{1}{(\sigma_{y0}^{22})^2} - \frac{1}{(\sigma_{y0}^{33})^2}\right]$$
$$G = \frac{1}{2}\left[\frac{1}{(\sigma_{y0}^{11})^2} + \frac{1}{(\sigma_{y0}^{33})^2} - \frac{1}{(\sigma_{y0}^{22})^2}\right]$$
$$H = \frac{1}{2}\left[\frac{1}{(\sigma_{y0}^{22})^2} + \frac{1}{(\sigma_{y0}^{33})^2} - \frac{1}{(\sigma_{y0}^{11})^2}\right]$$

In the same manner, the parameters L, M and N are related to the yield shear stresses τ_{y0}^{12}, τ_{y0}^{13} and τ_{y0}^{23} according to

$$L = \frac{1}{2(\tau_{y0}^{12})^2} \qquad M = \frac{1}{2(\tau_{y0}^{13})^2} \qquad N = \frac{1}{2(\tau_{y0}^{23})^2}$$

Hence, the parameters of Hill's yield criterion may be determined from experiments. In the deviatoric plane, Hill's yield surface corresponds to an ellipse as indicated in Figure 2.5. This indicates that the yield stress is different in the principal directions [5].

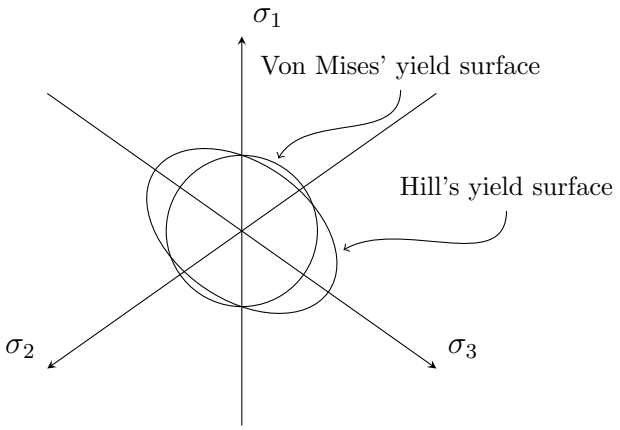

Figure 2.5: Von Mises' and Hill's orthotropic yield surface drawn in the deviatoric stress plane [5].

2.5 Isotropic hardening

The current yield stress, σ_y, may vary in three different ways. An increase with increasing plastic strains is called *hardening*, a decrease with increasing plastic strains

is called *softening*, whereas a yield stress that is the same for all plastic strains is called *ideal plasticity*.

A certain type of the hardening, where the yield surface is increased radially in size as the plastic strains are increased is called *isotropic hardening*. The initial yield surface is given by $f(\sigma_{ij}) = 0$, whereas the current yield surface has extra parameters $f(\sigma_{ij}, K) = 0$. Here, K is a set of one or more hardening parameters, defining the change of the initial yield surface.

For a von Mises material, the yield function is given by $f = \sigma_{eff} - \sigma_y = 0$, where σ_y is the *current yield stress*, defined as $\sigma_y = \sigma_{y0} + K(\kappa)$. Hence, in this case K is a single parameter defining the increase of radius of the initial yield surface. In turn, the hardening parameter is dependent on some internal parameter κ. There are various ways of choosing this variable, but a common choice is the effective plastic strain rate, $\dot{\varepsilon}^p_{eff}$ defined as $\dot{\varepsilon}^p_{eff} = \sqrt{\frac{2}{3}\dot{\varepsilon}^p_{ij}\dot{\varepsilon}^p_{ij}}$. The principle of isotropic hardening is shown in Figure 2.6, in the case of the von Mises yield surface.

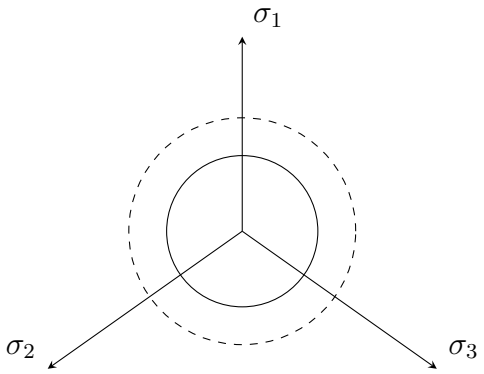

Figure 2.6: Isotropic hardening of a von Mises yield surface. The solid circle shows the initial yield surface whereas dashed shows the current yield surface [5].

The form of the isotropic hardening looks almost the same when it comes to orthotropic materials. However, there is no unambiguous way of choosing the initial yield stress σ_{y0}. Hence, the following definition is used instead

$$\sigma_{y0} = \sqrt{\frac{3}{2(F+G+H)}} \tag{2.6}$$

where the parameters F, G and H are the same as those introduced in Section 2.4 [5].

2.6 Finite element method

The finite element method is derived by using the strong form of the of equation of motion (momentum equation)

$$\sigma_{ij,j} + b_i = \rho \ddot{u}_i \tag{2.7}$$

Here, $\sigma_{ij,j}$ denotes divergence of the Cauchy stress tensor, b_i the body forces, ρ the density and $\ddot{u}_i$ the acceleration. The first step of the derivation consists of finding the weak form of the equation of motion. For this purpose, the arbitrary weight function v_i is introduced. Multiplication of the weight function and the equation of motion provides

$$v_i \sigma_{ij,j} + v_i b_i = v_i \rho \ddot{u}_i$$

The equation is then integrated over the entire domain of the body, i.e. the volume

$$\int_V v_i \sigma_{ij,j} dV + \int_V v_i b_i dV = \int_V v_i \rho \ddot{u}_i dV$$

Next, use is made of the Green-Gauss theorem provided by e.g. Ottosen & Petterson (1992), which applied to the first term in the integrated equations of motion, yields

$$\int_A v_i \sigma_{ij} n_j dA - \int_V v_{i,j} \sigma_{ij} dV + \int_V v_i b_i dV = \int_V v_i \rho \ddot{u}_i dV$$

This is the weak form of the equations of motion. Cauchy's principle may be recalled from Section 2.1 as well so that the traction vector may be introduced as $t_i = \sigma_{ij} n_j$. In order to formulate the finite element method, use must first be made of the *Voigt notation* [6]. By using this notation, the stress tensor σ_{ij} and weight function divergence $v_{i,j}$ are written in a more compact vector form as

$$\sigma_{ij} \rightarrow \tilde{\sigma}_i = \begin{bmatrix} \sigma_{11} \\ \sigma_{22} \\ \sigma_{33} \\ \sigma_{12} \\ \sigma_{13} \\ \sigma_{23} \end{bmatrix} \qquad v_{i,j} \rightarrow \tilde{v}_i = \begin{bmatrix} v_{11} \\ v_{22} \\ v_{33} \\ v_{12} \\ v_{13} \\ v_{23} \end{bmatrix}$$

Since v_i is arbitrary, it may be chosen in an infinite number of ways. In this case the Galerkin method is used. The Galerkin method suggests that the weight function should be chosen as

$$v_i = N_{ik} c_k \qquad \tilde{v}_i = B_{ik} c_k$$

where N_{ik} is the so called *shape function* and c_k is an arbitrary vector. The choice of N_{ik} is dependent on how the discretization is made, i.e. which types of elements that are used. The shape function is generally chosen as polynomials dependent solely on spatial coordinates and not time, i.e. $N_{ik} = N_{ik}(x, y, z)$. Moreover, B_{ik} is the gradient of N_{ik} [3]. Insertion into the equation of motion yields

$$\int_A c_k N_{ik} t_i dA - \int_V c_k B_{ik} \tilde{\sigma}_i dV + \int_V c_k N_{ik} b_i dV = \int_V c_k N_{ik} \rho \ddot{u}_i dV$$

Since c_k is both constant and arbitrary, the expression must be valid regardless of the choice of c_k, i.e.

$$\int_A N_{ik} t_i dA - \int_V B_{ik} \tilde{\sigma}_i dV + \int_V N_{ik} b_i dV = \int_V \rho N_{ik} \ddot{u}_i dV$$

The actual finite element approximation, in which the continuous body is split up in discrete elements is introduced next. An approximation of the displacement u_i as $u_i = N_{il} a_l \Rightarrow \ddot{u}_i = N_{il} \ddot{a}_l$, where a_l is the nodal displacement vector. In conclusion, the most general finite element formulation may hence be stated as

$$\left(\int_V \rho N_{ik} N_{il} dV \right) \ddot{a}_l + \int_V B_{ik} \tilde{\sigma}_i dV = \int_V N_{ik} b_i dV + \int_A N_{ik} t_i dA \tag{2.8}$$

Finally, if the following notations are introduced

$$\boldsymbol{M} = \int_V \rho N_{ik} N_{il} dV \qquad \boldsymbol{f}_{int} = \int_V B_{ik} \tilde{\sigma}_i dV \qquad \boldsymbol{f}_{ext} = \int_V N_{ik} b_i dV + \int_A N_{ik} t_i dA$$

the finite element formulation may be written in the following compact form [4] [5] [3]

$$\boldsymbol{M} \ddot{\boldsymbol{a}} = \boldsymbol{f}_{ext} - \boldsymbol{f}_{int} \tag{2.9}$$

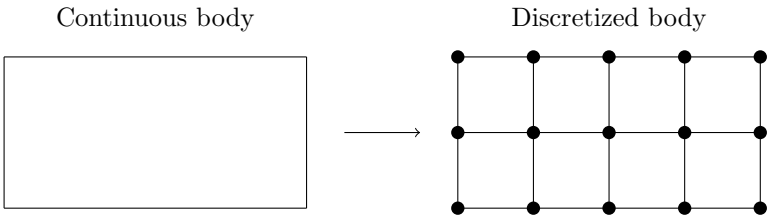

Figure 2.7: Finite element discretization with quadratic elements used as an example. Nodes are shown as dots.

In practice, in order to perform the integrations in Equation (2.8) elements are transformed into the *isoparametric domain*. Without going in to too much detail, a transformation to the isoparametric domain means that the integrands of an n-dimensional

integral of an arbitrary function f may be changed to n dimensional integrands ranging from $-1 \leq \xi_n \leq 1$. For a volume integral in three dimensions in particular, this means that

$$\int_V f(x_1, x_2, x_3)\ dV = \int_{-1}^{1}\int_{-1}^{1}\int_{-1}^{1} f(\xi_1, \xi_2, \xi_3)\tilde{J}\ d\xi_1 d\xi_2 d\xi_3$$

where $\tilde{J}$ is the mapping of the volume between different domains. In turn, the transformed integral must be determined in some manner. The transformation may be complex, whereby numerical integration is usually utilized. By doing so, the integral in the isoparametric domain may be approximated as

$$\int_{-1}^{1}\int_{-1}^{1}\int_{-1}^{1} f(\xi_1, \xi_2, \xi_3)\tilde{J}\ d\xi_1 d\xi_2 d\xi_3 \approx \sum_{k=1}^{l}\sum_{j=1}^{m}\sum_{i=1}^{n} f(\xi_1^i, \xi_2^j, \xi_3^k)\tilde{J}\ H_i H_j H_k$$

and ξ_1^i, ξ_2^j and ξ_3^k are fixed coordinates in the isoparametric domain, also known as *integration points* or *Gauss points*. Moreover, H_i, H_j and H_k are weight factors. The actual values of integration points and weigth factors are given by e.g. Ottosen & Petterson (1992). The values are also dependent on which type of elements that are used. It should be noted that the integration points do not coincide with the element nodes. The consequence of this is that whereas displacements are determined at the element nodes, element stresses are calculated at the integration points [3].

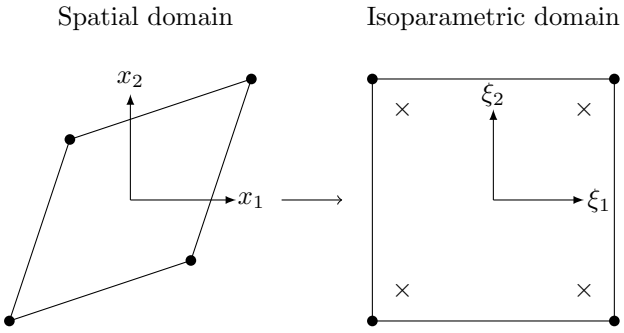

Figure 2.8: Transformation of a four node element from spatial dimensions to isoparametric domain. Nodes are shown as dots, whereas integration points are shown as crosses [3].

2.7 Explicit time integration

By explicit methods is meant that proceeding states are taken solely as a function F of the preceeding state, i.e. $S(t + \Delta t) = F(S(t))$. This approach will be used in this

case. From the finite element formulation in Equation (2.9), the following equation was obtained

$$\boldsymbol{M}\ddot{\boldsymbol{a}} = \boldsymbol{f}_{ext} - \boldsymbol{f}_{int}$$

By multiplying with $\boldsymbol{M}^{-1}$ from the left, the accelerations may hence be calculated as

$$\ddot{\boldsymbol{a}} = \boldsymbol{M}^{-1}(\boldsymbol{f}_{ext} - \boldsymbol{f}_{int})$$

assuming that $\boldsymbol{M}$ is invertible. In this case it is assumed to be diagonal and therefore trivially invertible.

The acceleration may change with time i.e. $\ddot{\boldsymbol{a}} = \ddot{\boldsymbol{a}}(t)$. Due to the fact that an explicit solution should be used, time steps, or *increments* must be used to account for the change with time. The current increment is denoted i, the previous $i-1$ and the next $i+1$. It should be noted that the index i is not used for tensor notations in this Section.

In order to find the velocities and displacements, the acceleration must hence be integrated over time in some manner. In this case, a second order central difference method is used for this purpose according to

$$\ddot{\boldsymbol{a}}_i = \frac{d^2\boldsymbol{a}_i}{dt^2} \approx \frac{\boldsymbol{a}_{i+1} - 2\boldsymbol{a}_i + \boldsymbol{a}_{i-1}}{\Delta t^2}$$

where Δt is the time increment. The expression may be rewritten somewhat to

$$\frac{\boldsymbol{a}_{i+1} - 2\boldsymbol{a}_i + \boldsymbol{a}_{i-1}}{\Delta t^2} = \frac{1}{\Delta t}\left(\frac{\boldsymbol{a}_{i+1} - \boldsymbol{a}_i}{\Delta t} - \frac{(\boldsymbol{a}_i - \boldsymbol{a}_{i-1})}{\Delta t}\right)$$

Now, if the time increments are not the same, i.e. $\Delta t_i \neq \Delta t_{i+1}$ the formulation takes a slightly different form

$$\ddot{\boldsymbol{a}}_i = \frac{1}{\frac{\Delta t_{i+1} + \Delta t_i}{2}}(\dot{\boldsymbol{a}}_{(i+\frac{1}{2})} - \dot{\boldsymbol{a}}_{(i-\frac{1}{2})}) \tag{2.10}$$

where $\dot{\boldsymbol{a}}_{(i+\frac{1}{2})}$ and $\dot{\boldsymbol{a}}_{(i-\frac{1}{2})}$ are so-called midpointincrements, defined as

$$\dot{\boldsymbol{a}}_{(i+\frac{1}{2})} = \frac{\boldsymbol{a}_{i+1} - \boldsymbol{a}_i}{\Delta t_{i+1}} \qquad \dot{\boldsymbol{a}}_{(i-\frac{1}{2})} = \frac{\boldsymbol{a}_i - \boldsymbol{a}_{i-1}}{\Delta t_i} \tag{2.11}$$

By doing this change, a modified central difference scheme is obtained where the acceleration is full central difference, whereas the velocities are not. A visualization of the method may be seen in Figure 2.9. If the midpointincrement from (2.10) is solved for, the following is yielded

$$\dot{\boldsymbol{a}}_{(i+\frac{1}{2})} = \dot{\boldsymbol{a}}_{(i-\frac{1}{2})} + \frac{\Delta t_{i+1} + \Delta t_i}{2} \ddot{\boldsymbol{a}}_i \tag{2.12}$$

From (2.11) it is possible to solve displacements of increment $i+1$ as well

$$\boldsymbol{a}_{i+1} = \boldsymbol{a}_i + \Delta t_{i+1} \dot{\boldsymbol{a}}_{i+\frac{1}{2}} \tag{2.13}$$

and by using linear interpolation it is possible to extract the velocities as

$$\dot{\boldsymbol{a}}_{i+1} = \dot{\boldsymbol{a}}_{1+\frac{1}{2}} + \frac{\Delta t_{i+1}}{2} \ddot{\boldsymbol{a}}_{i+1} \tag{2.14}$$

So, to summarize the algorithm, it first calculates the acceleration at the current state $\ddot{\boldsymbol{a}}_i$. Then, midincrement $\dot{\boldsymbol{a}}_{(i+\frac{1}{2})}$ is calculated using (2.12). Finally, displacements and velocities are calculated using (2.13) and (2.14), respectively.

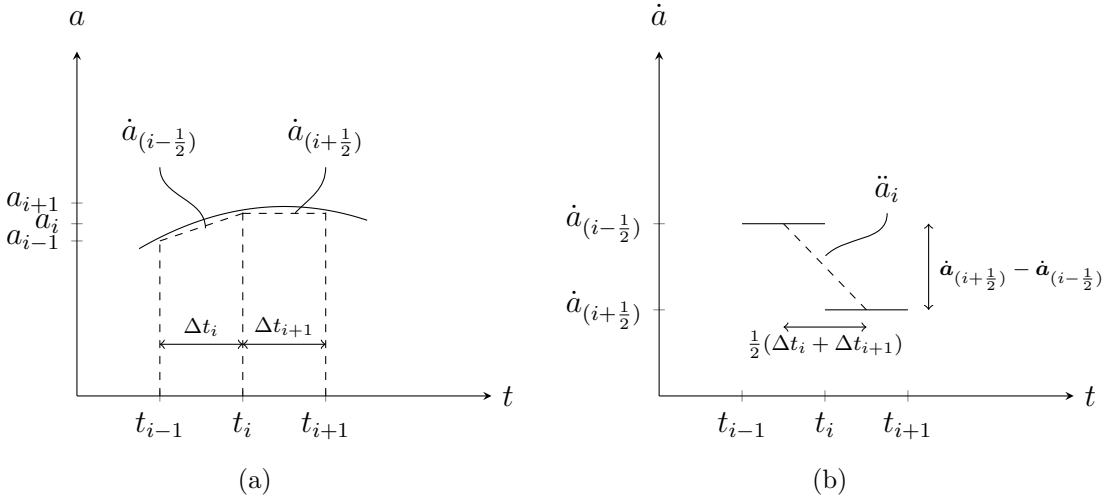

Figure 2.9: Principle of the modified central difference time integration. a) Determination of the midincrements. b) Determination of acceleration.

This method is stable if the time increments Δt are chosen small enough. The size of the time increments is dependent on the maximum eigenfrequencies of the system ω_{max}, since even the most rapid oscillations must be resolved. Mathematically, the condition of the time increment may be stated as

$$\Delta t \leq \frac{2}{\omega_{max}} \tag{2.15}$$

which numerically may be estimated according to

$$\Delta t \approx \frac{L_{min}}{c_d} \tag{2.16}$$

Here, L_{min} is the smallest element side and c_d the dilational wave speed, i.e. the speed at which information is transmitted in the system. Without going into the details of the definition of c_d, it is possible to reformulate the stable time increment as

$$\Delta t \approx \zeta L_{min}\sqrt{\rho} \tag{2.17}$$

where ζ is some constant and ρ the density. Thus, the stable time increment is essentially proportional to the element size and element mass. It may hence be noted that the time increment may be manipulated by increasing the element density, something called *mass scaling*. In this manner, it is possible to compensate for smaller element sizes by increasing the mass of the element [1].

2.8 Contacts

Consider two bodies M, and S that are in contact. Here, M stands for *master* and S for *slave*, and the master body defines the normal at the contact interface. These bodies are not physically allowed to penetrate each other, but for so-called *penalty contact* they are numerically allowed to do so. The penetration is provided by the *penetration function* g_N introduced as

$$g_N = \begin{cases} (x_i^S - x_i^M)n_i & \text{if } (x_i^S - x_i^M)n_i < 0 \\ 0 & \text{otherwise} \end{cases} \tag{2.18}$$

This means that if g_N is less than zero, the slave surface will penetrate the master surface. If this is the case, a large force t_N opposing the penetration, i.e. in the n_i direction is introduced. The force is defined as $t_N = P_N g_N$, where P_N is the so-called *penalty factor*. The contact force itself, denoted t_i^c, is then expressed as $t_i^c = t_N n_i$ [4].

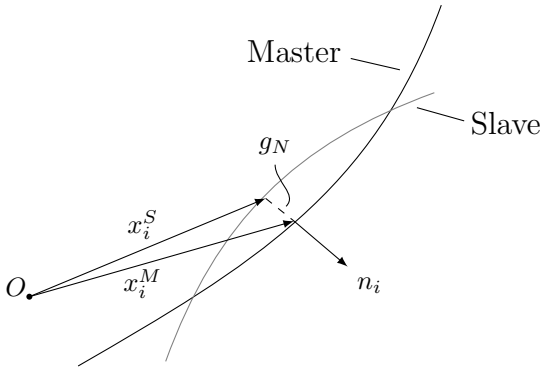

Figure 2.10: Principle of contact. The master surface (black) is penetrated by the slave surface (gray) so that $g_N < 0$. The surface normal n_i is taken from the master surface.

As seen in Equation (2.8), forces acting on the body have already been introduced, so the contact forces in this case will be a contribution to the total forces. Hence, it is reasonable to express the contact forces as

$$\boldsymbol{f}_{contact} = \int_{A^c} N_{ij} P_N g_N n_i dA \tag{2.19}$$

where A_c is the surface in contact. In conclusion, the finite element formulation may be written in the following manner [4]

$$\boldsymbol{M\ddot{a}} = \boldsymbol{f}_{ext} + \boldsymbol{f}_{contact} - \boldsymbol{f}_{int} \tag{2.20}$$

2.9 Hydrostatic fluid interactions

A cavity is a hollow space in some structure containing some sort of fluid, either gas or liquid. The main assumption of the cavity is that the pressure is constant at every facet surrounding it. If the cavity fluid is a compressible liquid, the definition of bulk modulus may provide a linear relation between the volume V and pressure p of the cavity, stated as

$$p = -K \left(\frac{V(p,T) - V_0(T)}{V_0(T_0)} \right) \tag{2.21}$$

Here, K is the bulk modulus, V the current volume and V_0 the initial volume. T and T_0 are current and initial temperatures, respectively. As seen, the pressure will

depend on the temperature of the cavity, which is also assumed to be uniform at every facet. Since the initial volume is assumed to be known, only the current volume $V(p, T)$ needs to be determined.

Next, introduce the numerical volume as $\overline{V}$. The numerical volume is the volume enclosed in the discretized cavity. It is determined by putting a reference point located inside the cavity. By connecting the nodes of the containing elements to this point, it is possible to create pyramidal elements with five nodes, containing a volume. By means of linear algebra, the volume of this element may be calculated. The total cavity volume is then determined by summing the volumes of each element.

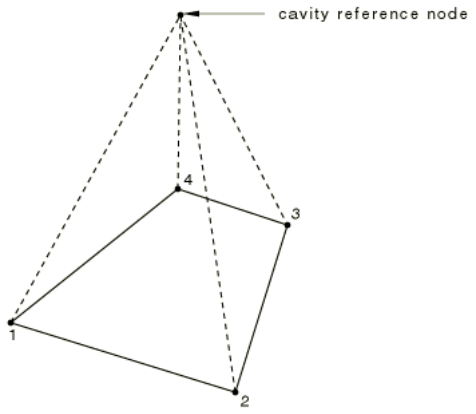

Figure 2.11: Determination of numerical volume $\overline{V}$ using a reference point and pyramidal elements [1].

By using the numerical volume as an approximation of the actual cavity volume, i.e. by using the constraint $V - \overline{V} = 0$, the cavity pressure, applied to every element, is found using Equation (2.21) [1].

2.10 Energy balance

The second law of thermodynamics, i.e. that energy may neither be destroyed nor created, must always apply. Another way of stating this is that the energy in the system must be constant. When it comes to the energy balance of systems with just mechanical and thermal properties, the total energy E_{tot} may be expressed as

$$E_{tot} = E_I + E_V + E_{FD} + E_{KE} + E_{IHE} - E_W - E_{PW} - E_{CW} - E_{MW} - E_{HF} \quad (2.22)$$

where E_I is the internal energy, E_V the viscous energy dissipation, E_{FD} the frictional energy dissipation, E_{KE} the kinetic energy, E_{IHE} internal heat energy, E_W the external

load work, E_{PW}, E_{CW}, E_{MW} the work done by contact and constraint penalties as well as propelling added mass, and finally E_{HF} is the external heat flux work. This sum should be constant at all times.

In turn, the internal energy may be divided in components as well

$$E_I = E_E + E_P + E_{CD} + E_{DMD} + E_{DC} + E_{FC} + E_A \tag{2.23}$$

Here, E_E, E_P and E_{CD} are elastic, plastic and viscoelastic strain energies. The two latter strain energies are dissipative. E_{DMD} and E_{DC} are damage and distortion control dissipation, respectively. The final contribution E_{FC} is a special type of energy, which is only present when hydrostatic fluid interactions are included. It is the fluid cavity energy caused by the work done by the combination of pressure and volume change of the cavity [1].

E_A is the so-called artificial strain energy. The purpose of the artificial strain energy is to compensate for *spurious zero energy modes*. More in detail, these modes are caused by non-rigid body displacements, i.e. a certain pattern of nodal displacements that do not form any strain energy [3]. This is a purely numerical phenomenon, caused by *reduced integration*.

Reduced integration means that less integration points than required for an exact integral solution are used to calculate stresses in the element. For four node elements for instance, so-called hourglass patterns containing zero energy modes may appear. It is the prevention of this hourglassing that will form the artificial strain energy, E_A, so if this energy is large in magnitude it is an indication of that reduced integration may not be suitable.

Full integration, i.e. using sufficient integration points to evaluate the integral exactly, will on the other hand provide a structure that is too stiff [3].

CHAPTER 3

Physical testing

In this chapter, a presentation of the various physical tests on the packages is provided. The setup and execution of the tests are explained.

A specific set of packages are used throughout the thesis. These contain a volume of 220 ml. The packages were stored on pallets until they were tested. The physical testing was conducted in a climate controlled laboratory, with a temperature of 23° C and 50% relative humidity and the packages were conditioned for at least than 24 hours before the experiments were conducted.

The physical tests were conducted in the form of compression tests. The compression tester of model Zwick/Roell Z005 at Tetra Pak was used for this purpose. It consists of two horizontal parallel metal plates where the top plate is brought towards the bottom plate. The test object is placed between these plates. A load unit registers the reaction force on, as well as the displacement of the top plate. An image of the Zwick/Roell Z005 machine may be seen in Figure 3.1 below.

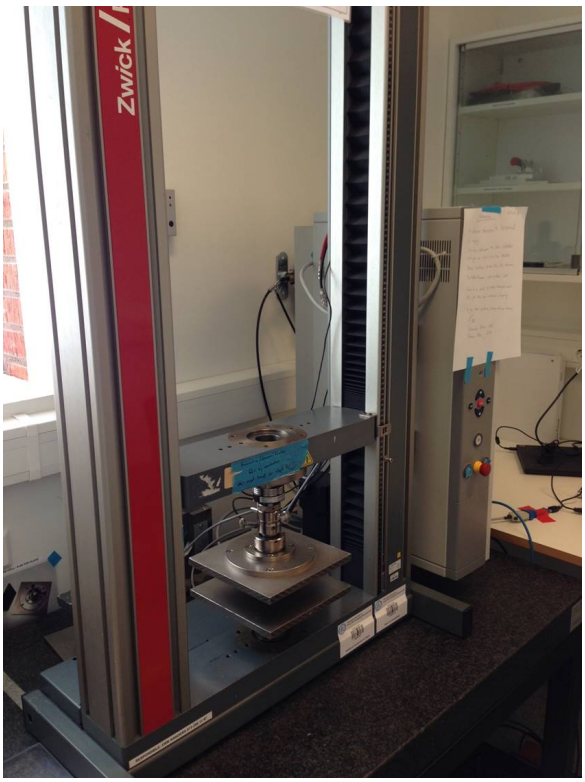

Figure 3.1: Image of the Zwick/Roell Z005 compression tester used for physical tests.

3.1 Single package compression tests

A compression test of a single package consists of two steps, preloading and rupture loading. In the preloading step, the top plate is first lowered with a speed of 100 mm per minute until a certain reaction force is measured. This force depends on the package type, but in this case it is set to 150 N. Once this load level is obtained, the rupture load step is initiated. Here, the speed of the top plate is reduced to 5 mm per minute. The top plate is continuously lowered until the package ruptures, which is considered to be when the load is reduced by 70%. What happens to the package itself at this point is that a tear appears so that the contained fluid will exit the package effortlessly. Due to large variations in package shape, 30 different packages were used in the tests.

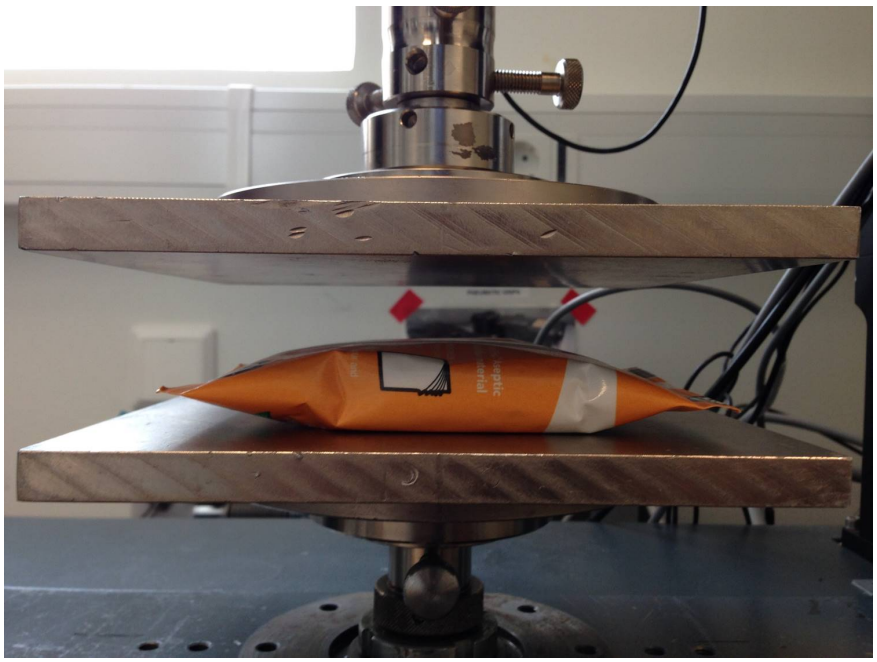

Figure 3.2: Test setup for single package testing. A package is placed between the top and bottom plates of the Zwick. In the actual test the package was placed in a plastic bag to protect the equipment.

3.2 Double package compression tests

The double package compression tests were conducted in the same manner as described in the section above. However, two packages were used instead. The two packages were placed with different shortside overlaps, being 12.5%, 25% and 50%. The two packages are denoted P1 and P2, with the definition that P1 is in the bottom with P2 laying on top of it. The packages were placed so that the bottom of P2 was overlapping the top of P1. In other words, the bottom end of P1 as well as the top end of P2 were free ends. 30 tests were conducted for each overlap, resulting in a total of 90 tests. In order to check the influence on the placing of the package in the bottom, 5 additional tests where P1 and P2 switched place were conducted. The preload step was set to end at 150 N.

Figure 3.3: Test setup for overlap testing. P1 is put in the bottom (left in image) and P2 on top (right in image). 50% overlap is shown in the image.

3.3 Internal stiffness calibration

In order to compare results from the virtual and physical compression tests, the internal spring stiffness of the load cell has to be taken into account. The top plate will be displaced relative to the displacement measuring device due to its load, which is something that is not taken into account in the data output. Hence, a calibration is required.

The calibration data is taken from previous tests conducted at Tetra Pak. The test was conducted so that the top plate was brought to to the bottom plate, and the reaction force of the top plate was measured. Thus, the plate itself was not able to move, although the measuring device could. Hence, a relative displacement at each load point could be obtained. The results of this test may be seen in Figure 3.4.

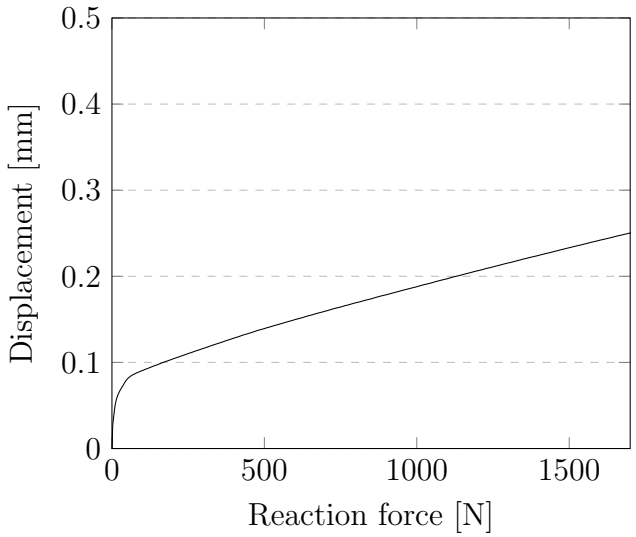

Figure 3.4: Relative displacement of top plate and measuring device as a function of the reaction force [7].

This means that the load cell will experience some compression hence yielding too large displacements in the data. Therefore, in order to compare virtual and physical data, the displacement values of each load point in this test had to be subtracted from the data acquired in the compression tests, i.e.

$$d_{plate} = d_{measured} - d_{LC}(RF) \tag{3.1}$$

Here, the internal displacement of the load cell d_{LC} is a function of the reaction force RF at each load point. For all results where physical and virtual data are compared, this compensation has been made.

CHAPTER 4

Models

This section describes how the physical tests are modeled using the finite element method. Assumptions and simplifications of the real situation will be explained, and the model setups will be described and shown. All models are created and solved using the commercial software Abaqus 2017.

4.1 Single package virtual compression test

4.1.1 Material models

As mentioned in the introduction, the material of the Tetra Pak packages consists of six plies being polyethylene, cardboard, polyethylene, aluminium and finally a double layer of polyethylene, as seen in Figure 1.2. These materials all have different properties, which means that they will also have be modeled using different material models. The material models has been previously calibrated and validated by Tetra Pak.

All plies consisting of polyethylene use the same material model, although the individual parameters differ somewhat. As polyethylene is a polymer, it is modeled by Arruda-Boyce hyperelasticity. In addition, plasticity is also considered in the form of isotropic von Mises hardening, initiated by von Mises' yield criterion.

The paperboard is considered to be orthotropic, where the direction dependencies have been previously determined experiments. Also the paperboard utilizes isotropic hardening and Hill's yield criterion, where constants F, .., N also are determined experimentally.

The aluminium foil is orthotropic, even though there is only a slight direction dependence of the material stiffness. Hence, the material will be considered to be more or less isotropic. However, plasticity is still modeled using Hill's yield criterion combined with isotropic hardening.

In order to model the multiply layering, the materials are stacked as a composite material, i.e. without any possibility of delamination. The LS zone is simply approximated by double stacking the composite.

The reason for using isotropic hardening is that it is suitable for continuous loading, such as compression tests, where unloading is not present.

4.1.2 Geometry and mesh

The virtual compression model consists of top and bottom plates as well as a Tetra Fino® Aseptic package. The geometry of the package in the model was taken as an orphan mesh from a previously existing forming model. The package is completely covered by the plates, as is also the case for the physical tests. In order to reduce the computational effort, symmetry is considered and only half of the package and plates are included in the model. The setup is shown in Figure 4.1.

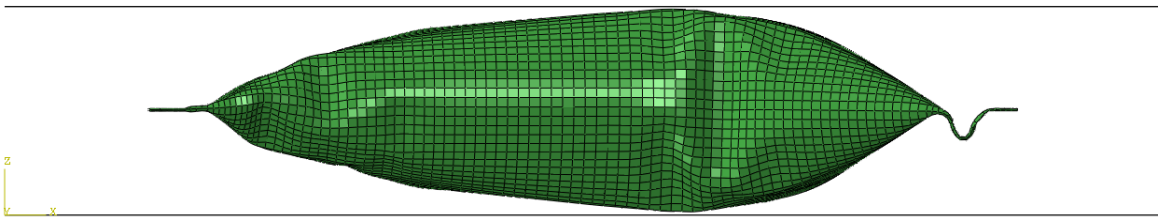

Figure 4.1: Model of the single package in compression. The package is put between the top and bottom plates. The package geometry was taken as an orphan mesh from a forming model.

Both of the plates are considered to be rigid, which is a reasonable assumption due to the fact that metal is much stiffer than paperboard. Hence, they were meshed using rigid elements, in Abaqus denoted R3D4, i.e. three dimensional four node elements. Two different types of elements were used for the package, S4 and S4R. The former are four node shell elements with 2x2 integration points. The latter are also four node

shell elements, but with reduced integration, thus only providing 1x1 integration point. Shell elements are also associated with a thickness, here taken as the total material thickness.

Two mesh sizes are used. The average mesh size in the first case is about 2 mm and refined to about 1 mm near the seals. The second mesh has a seed of 0.5 mm overall, and a refinement to 0.5x0.25 mm near the seals. The latter is referred to as the fine mesh.

4.1.3 Constraints

Only two constraints are used in the model. The ends of the package corresponding to TS are tied together using constraints on the surface nodes. Thus, the nodes in this region are not allowed to move relative to each other. This is a reasonable assumption due to the fact that the seals are not the rupture areas of the package, c.f. Section 1.3. A tie constraint of a seal is shown in Figure 4.2.

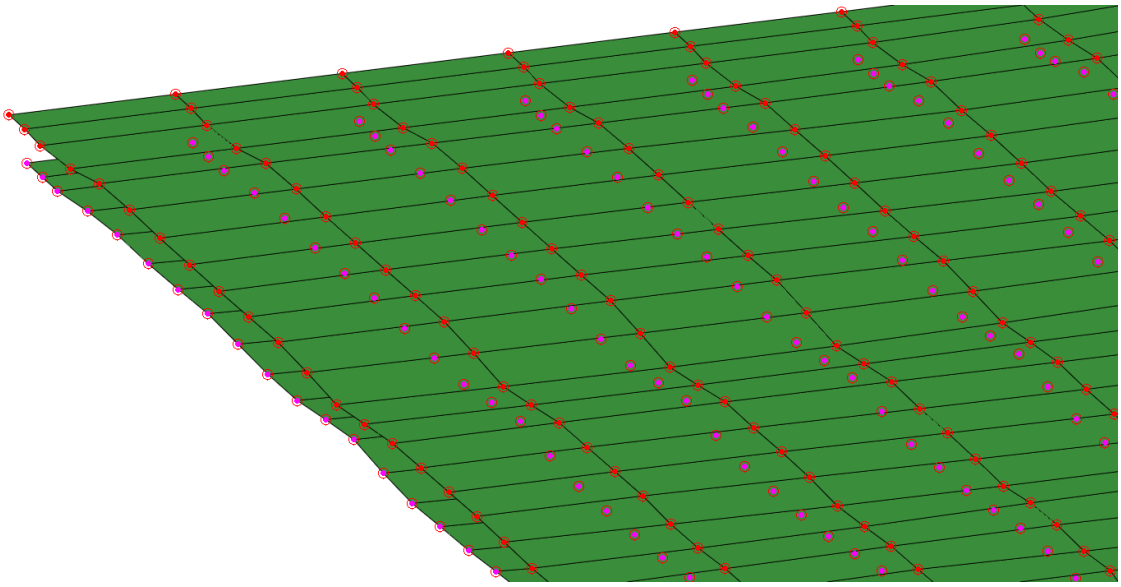

Figure 4.2: Constraints used for the TS seals. Marked nodes are unable to move relative each other. Note that the package thickness is not displayed.

The fluid contained in the package also poses a constraint on the system. As the package is completely filled with water, and water is nearly incompressible, a requirement will be that the package volume remains nearly constant. For this purpose a cavity interaction, which is described in Section 2.9, is used. The reason for including compressibility is simply numerical. This is a hydrostatic condition, which does not include dynamic effects of the water. In this case, this is not considered to be an issue, since the compression is slow enough so that all dynamic effects of the fluid may be

neglected.

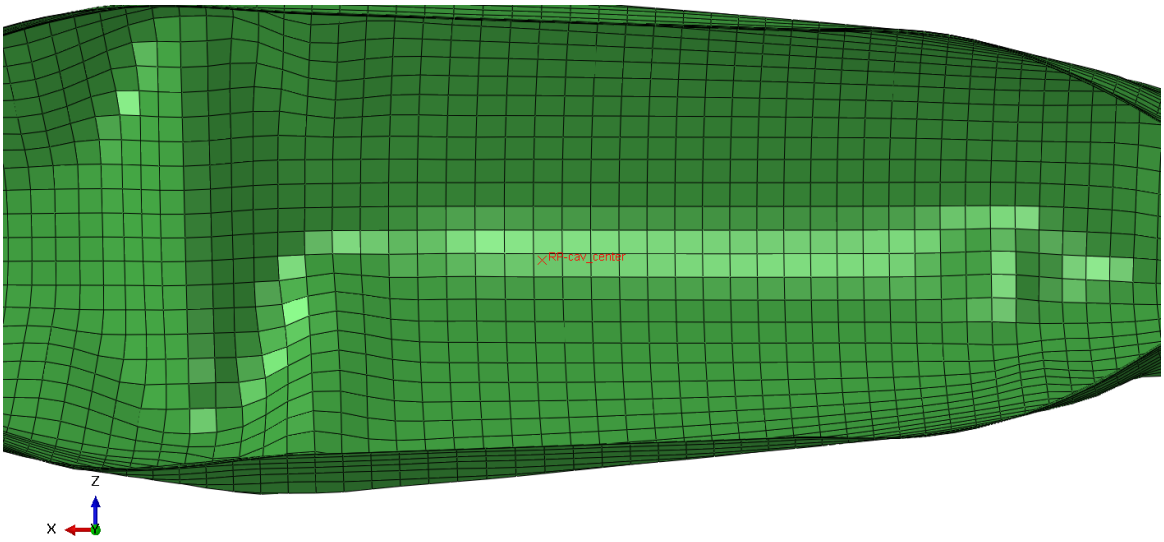

Figure 4.3: Reference point of the cavity marked in red. The nodes of all shell elements are virtually connected to this point in order to calculate the cavity volume.

4.1.4 Contacts

Only three contact zones are present in this model. There is contact between the top and bottom plates and the package, as well as contact between the inner surfaces of the package. The interior contact will only be relevant initially, as the package will bulk up as it is loaded. Frictional penalty contact was used for the interior contact. Frictional penalty contact was also used for the tube-plate contacts, where the friction is only present to prevent the package from sliding.

4.1.5 Loads and boundary conditions

No loads are applied in this model. The system is thus completely displacement controlled. The displacement control is set by the top plate which is assigned a velocity boundary condition. The speed is not set to match reality due to the fact that the simulation time then would be too extensive. Hence, the speed of the top plate is increased from 100 mm/min to 1000 mm/min during the preload step, and from 5 mm/min to 50 mm/min during the rupture load step, compared to the physical tests. Thereby, the time duration of the virtual test is reduced by a factor 10. The reason for not increasing the speed more than this is that the dynamic effects may become of greater importance, thus influencing the result. In reality, a faster speed

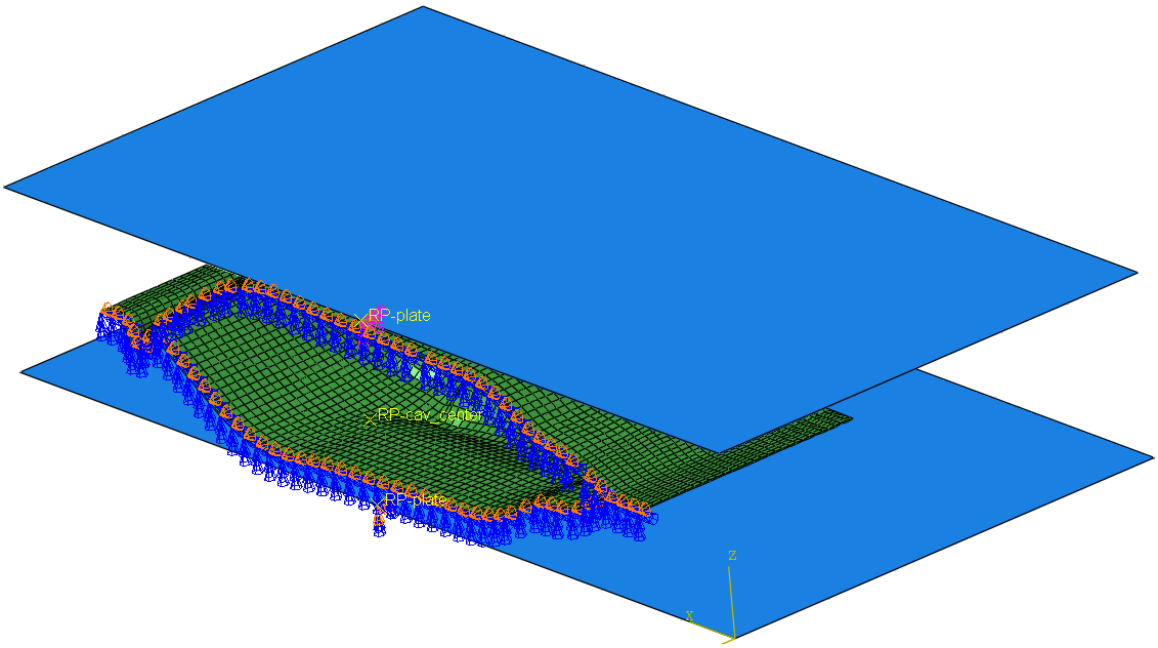

Figure 4.4: Symmetry boundary condition applied to the edge of the package.

reduces the data resolution due to requirements on increased sampling rate. In the model, however, this is not an issue since the sampling rate may be set arbitrarily.

The bottom plate is locked in all degrees of freedom so that it will not move as the package is compressed. Since only half the package and plates are used in the model, a symmetry boundary condition preventing movement orthogonal to the plane is introduced. This is shown in Figure 4.4.

An initial state is also set to the package. In this case the material state, i.e. stresses, strains, plastic strains, damage etc. from the finished package in the forming process will be applied to the package in the first increment in this model. Hence, if any type of defects or damages have been introduced already in the forming process, they will be taken into consideration in the compression test as well.

4.1.6 Solution scheme

The virtual compression is solved with an explicit time integration method, c.f. Section 2.7. There are several reasons for using the explicit method. One reason is that it is not possible in Abaqus to rename, move or duplicate parts that use an initial state condition for implicit methods. Another reason is that convergence of contacts, partially between the package and the plates, and partially between the interior parts of the package, is difficult to obtain.

Due to long simulation times, *mass scaling* is used as well. Thus, the simulation will

complete faster. In this model, a factor of 32 is used for this purpose. Although this is a large factor, comparisons to a simulation without any mass scaling showed no difference in results. The reason for this is that the problem is nearly static, whereby dynamic effects are negligible. These comparisons are not included in the report. A physical motivation for using mass scaling may also be considered, as extra weight of the water is to some extent included.

4.2 Double package virtual model

The only major difference of this model, compared to the single package model is that there is another package included. Also, both the top and bottom plates had to be widened, and the top plate had to be raised somewhat in order to fit the packages. Penalty contact between the two packages is also included. All geometries, meshes, contacts, boundary conditions etc. remain the same. However, only the S4 elements are used. The setup of the model may be seen in Figure 4.5.

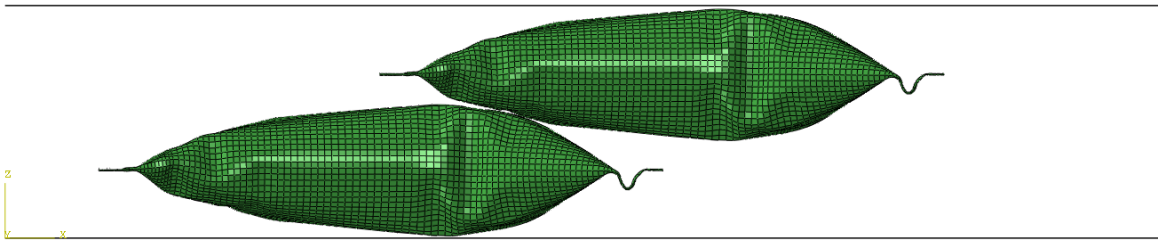

Figure 4.5: Setup of the double package virtual model. A 50% overlap is shown here.

As seen, the packages are ”levitating”. This will be negligible since there is no gravity. Various shortside overlaps, corresponding to those from the physical tests, are used in the model.

4.3 Package stacking virtual model

The only difference of this model, compared to the single package model is that there are several packages included. All geometries, meshes, contacts, boundary conditions etc. remain the same. However, only the S4 elements are used. The packages are stacked on top of each other using 100% OLL and OLS.

CHAPTER 5

Results

This section presents the results obtained in the thesis, both physical and virtual. The results are focused on package deformation, force-displacement data, the internal pressure and stress and strain distributions.

5.1 Single package physical compression tests

5.1.1 Deformation and fracture

The packages are deformed somewhat differently and will have different appearances after rupture. Typical appearances of both the shape of the package close to the failure load and of packages that have already failed are shown in the figures below. However, for Figure 5.1 the image is taken somewhat below the failure load in order to avoid rupture while taking the picture. Thus the package will not be fully inflated and some extra wrinkles may be present.

Figure 5.1: Deformation of the package during compression.

Figure 5.2: Appearance of a ruptured package seen from the outside. The package fails somewhere near the LS-area. Image shows a rupture at frontside bottom.

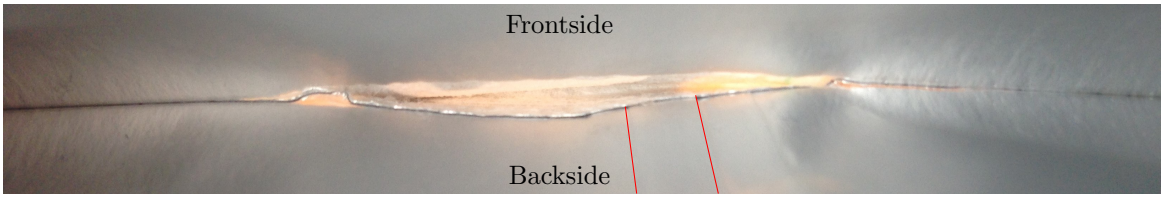

Figure 5.3: Appearance of a ruptured package seen from the inside. The package fails somewhere near the LS-area, which is marked in red. Image shows a rupture at frontside bottom.

5.1.2 Force-displacement data

The data obtained from the compression test is both force and displacement at failure, as well as data for the entire force-displacement curve. The average failure load and displacement, with corresponding standard deviations are also determined. These values are shown in Table 5.1.

	Avg	Std dev
Failure reaction force [N]	1498	95
Failure displacement [mm]	0.84	0.035

Table 5.1: Average loads and displacements at failure, with corresponding standard deviations for physical compression tests.

In addition, the rupture position, i.e. the location at which the packages fail was also noted. The rupture position was limited to one of the four positions described in the nomenclature. The rupture positions of the compression tests are shown in Table 5.2.

Position	Number
Frontside top	3
Frontside bottom	14
Backside top	5
Backside bottom	8

Table 5.2: Rupture location of packages in the test series.

The force-displacement data for each test was also obtained. The data collection was initiated in the rupture load step. Data for the 30 packages is shown in Figure 5.4 a). By using this data an average force-displacement curve could be constructed. The average curve simply uses the average value of the force in each displacement point. However, after a package ruptures, there will not be any more data recorded. Hence, when averaging the data, only the tests where packages had not yet failed were used for each displacement value. The average curve may be seen in Figure 5.4 b).

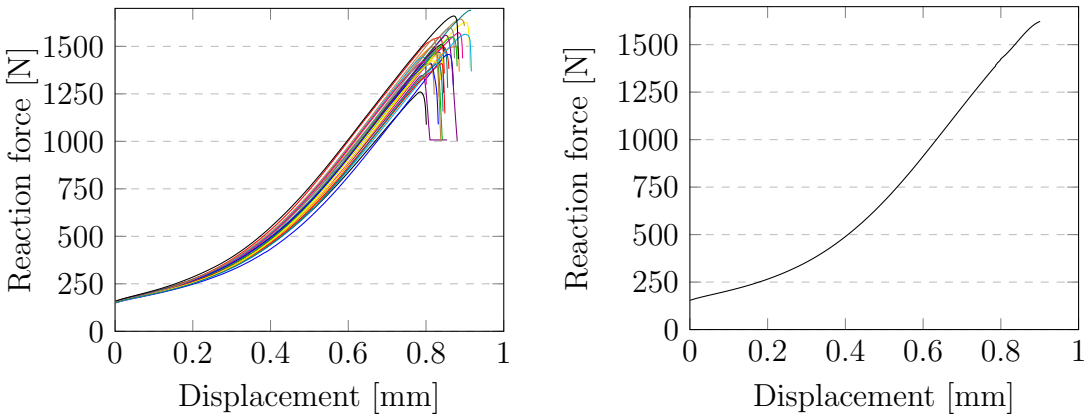

Figure 5.4: a) Force-displacement data of all 30 compression tests. b) Average force-displacement curve for compression tests.

5.2 Double package physical compression tests

5.2.1 Deformation and fracture

The packages are deformed somewhat differently and will have different appearances after they have ruptured. Typical appearances of both the shape of the package close

to the failure load and of packages that have already ruptured are shown in the figures below. However, for Figure 5.5 images are taken somewhat below the failure load in order to avoid rupture while taking pictures. Thus the packages will not be fully inflated and some extra wrinkles may be present.

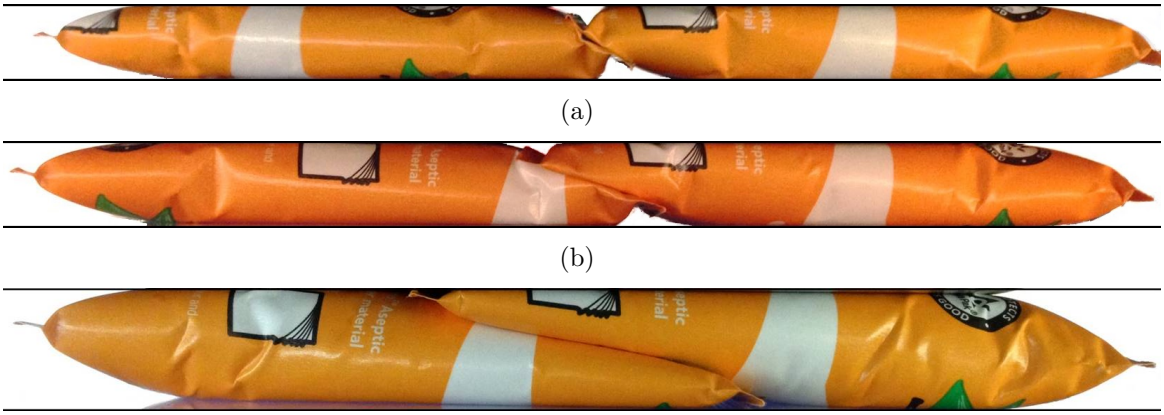

(a)

(b)

(c)

Figure 5.5: Deformation of packages with a) 12.5% b) 25% and c) 50% overlap.

Figure 5.6: Typical state after rupture for overlap test.

Figure 5.7: Rupture of P1 after compression test using overlap.

5.2.2 Force-displacement data

The data obtained from the compression test is both force and displacement at failure, as well as data for the entire force-displacement curve. The average failure load and

displacement, with corresponding standard deviations are also determined. Data was collected for each overlap and the values are shown in Table 5.3.

	Avg			Std dev		
	12.5%	25%	50%	12.5%	25%	50%
Failure reaction force [N]	2753	2525	1756	228	200	166
Failure displacement [mm]	1.97	2.02	1.93	0.12	0.10	0.16

Table 5.3: Average loads and displacements at failure, with corresponding standard deviations for physical compression tests of two packages with 12.5%, 25% and 50% overlap.

In addition, it was noted which package that ruptured, i.e. either P1 or P2. The corresponding rupture position was also noted. The rupture positions obtained in the compression tests are shown in Table 5.4.

	12.5%		25%		50%	
	P1	P2	P1	P2	P1	P2
Frontside bottom	21	0	28	0	26	0
Frontside top	0	1	0	1	0	1
Backside top	0	0	0	0	0	1
Backside bottom	0	0	1	0	2	0

Table 5.4: Rupture positions of the packages in the test series for each overlap, respectively.

Each overlap has a test series of 30 individual tests. The exception is the 12.5% case, since a misalignment of the testing equipment occurred mid-testing. Hence, only 22 of these tests could be used. Test data for the overlap tests is shown in Figure 5.8-5.10 a). The average curves may also be seen in Figure 5.8-5.10 b).

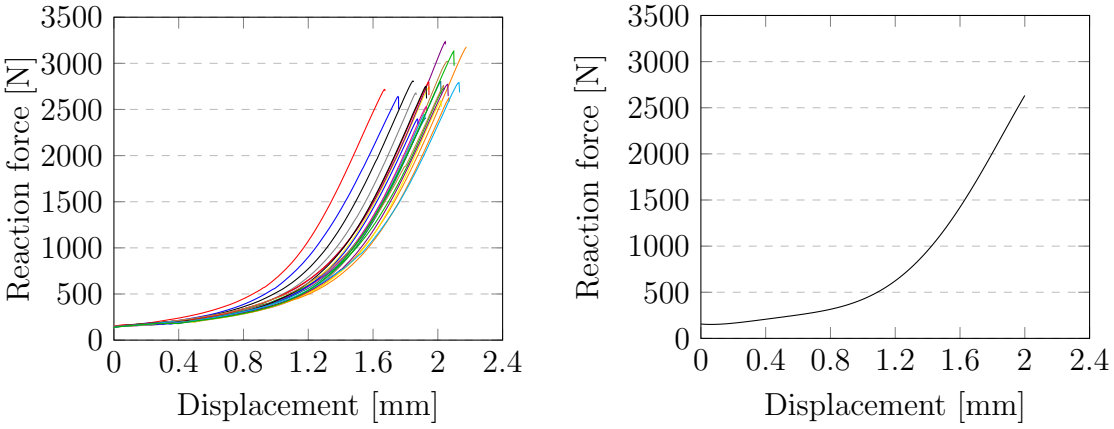

Figure 5.8: Reaction force as a function of displacement for two packages with 12.5% overlap.

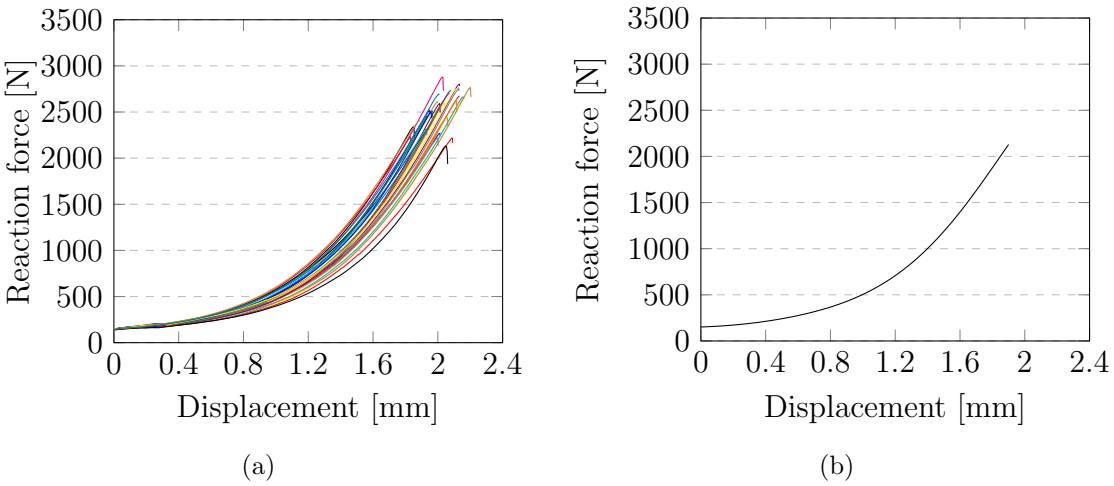

Figure 5.9: Reaction force as a function of displacement for two packages with 25% overlap.

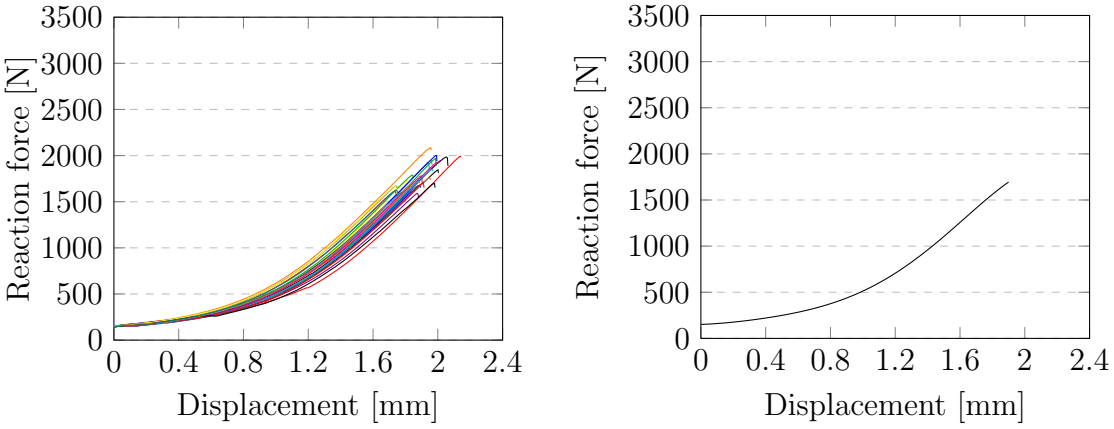

Figure 5.10: Reaction force as a function of displacement for two packages with 50% overlap.

In addition, the average curves of each overlap are plotted in the same image, as seen in Figure 5.11.

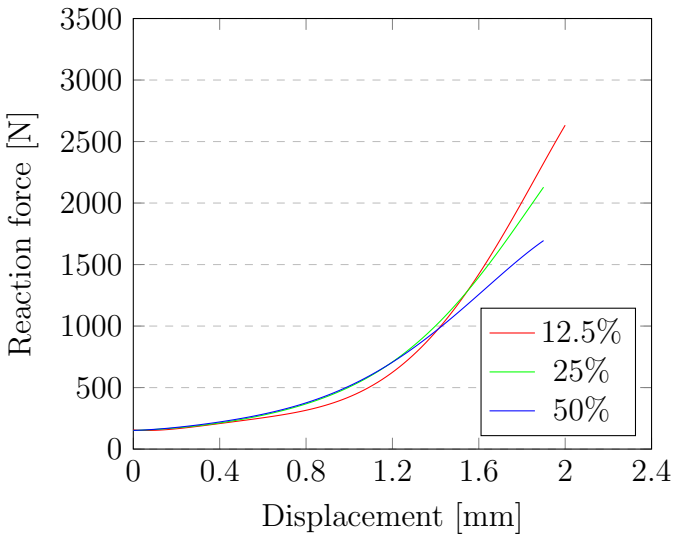

Figure 5.11: Average force-displacement curves for 12.5%, 25% and 50% overlap, respectively.

Data for the 5 additional tests where P1 and P2 has switched positions is not shown. Referring to Figure 5.6, the switched positions mean that P1 was still placed to the left, but on top of P2. There were no major differences in the force-displacment data, and all tests showed that the rupture position was frontside bottom of P1 (in this case placed on top).

5.3 Single package virtual compression tests

5.3.1 Deformation

In the virtual case, only the deformation during compression may be shown. The model has no fracture mechanics, whereby images of a ruptured package cannot be obtained. A deformed virtual package is shown in Figure 5.12.

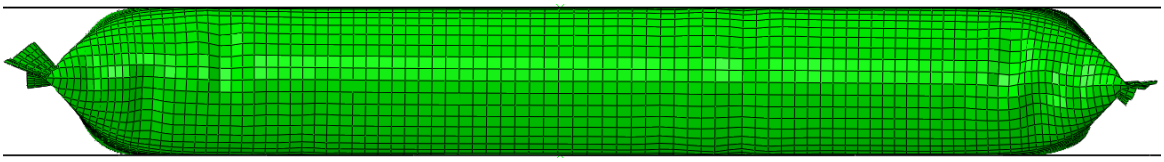

Figure 5.12: Deformation of a single package.

5.3.2 Force-displacement data

The calculated reaction force of the top plate as well as the displacement of the top plate is shown in Figure 5.13. Also shown dashed is the average curve of the physical testing.

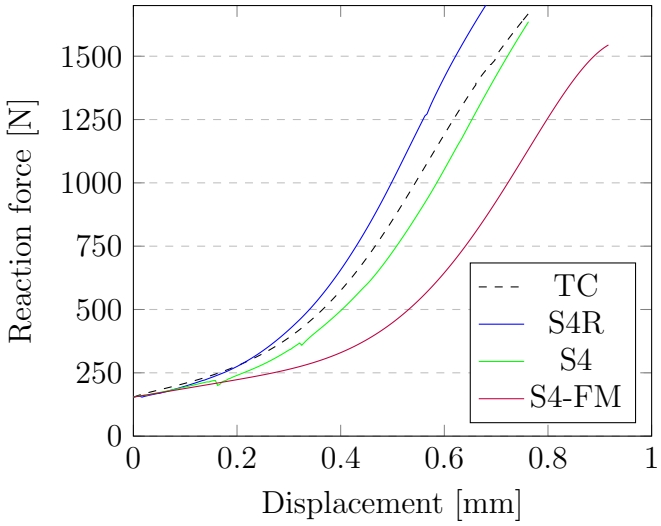

Figure 5.13: Results of virtual compression tests using S4 and S4R elements, as well as a finer mesh (FM). Also drawn is the calibrated average physical data (TC).

5.3.3 Pressure-force data

The internal cavity pressure of the package was obtained and plotted as a function of the reaction force of the top plate of the compression tester. This is shown in Figure 5.14.

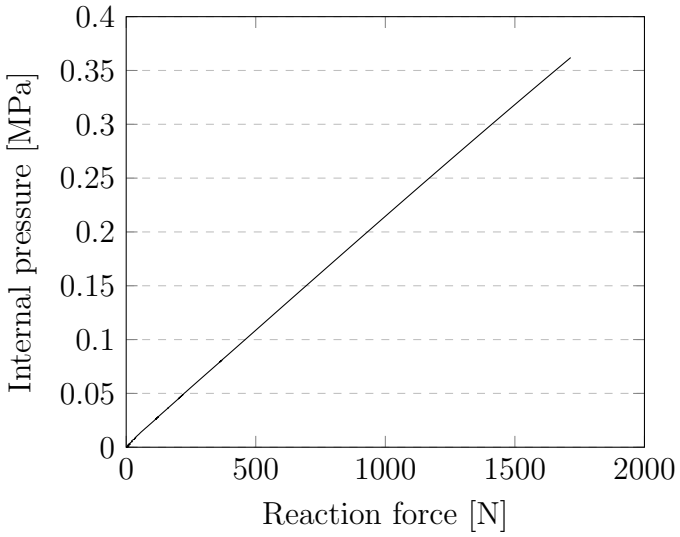

Figure 5.14: Internal pressure of the package as a function of reaction force.

5.3.4 Specification of views and directions

Stresses and strains in the case of virtual compression testing are shown in Section 5.3.5 to 5.3.10 for two specific views. These views are referred to as top and bottom, showing the inside of the package rather than the outside. In order to simplify understanding of how the views are specified, a reference to a physical package is shown in Figure 5.15.

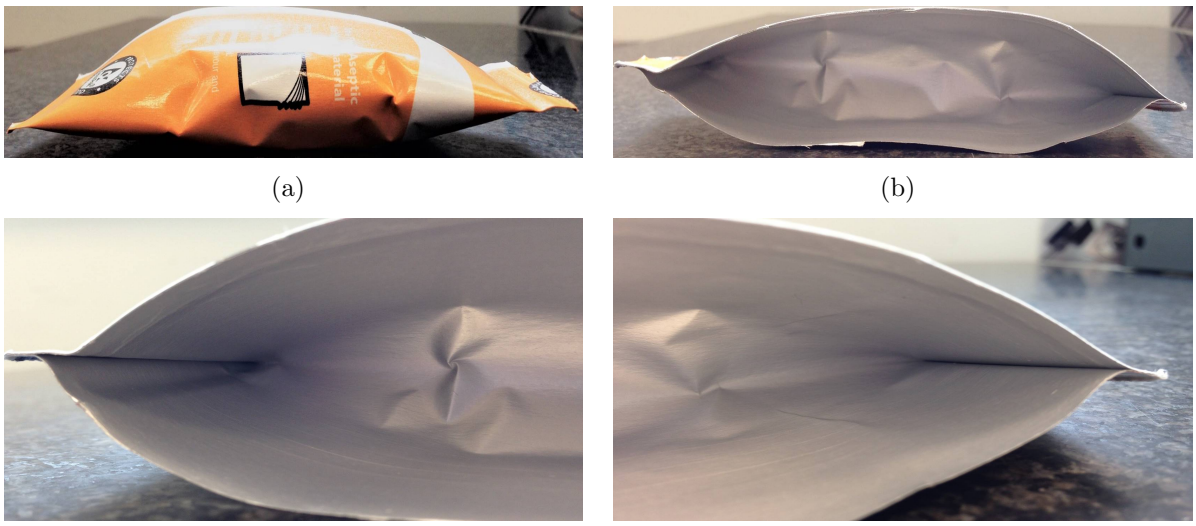

(a) (b) (c) (d)

Figure 5.15: a) Package positioned as in test. b) Package rotated 180 degrees about the vertical axis and cut in half. c) View referred to as top. d) View referred to as bottom.

It is also necessary to specify the directions in which stress and strain components are defined. The machine direction (MD) is defined as the direction parallel to LS and hence orthogonal to TS. In the same manner the cross machine direction (CD) is defined as the direction parallel to TS and hence orthogonal to LS. These notations are normally used at Tetra Pak, and they are derived from the way that the packaging material is manufactured and how it is oriented. The material also enters the filling machine in a way that orients the length direction of the package in MD. Hence, MD is here the length direction of the package and CD the width direction of the package. The directions are shown in Figure 5.16.

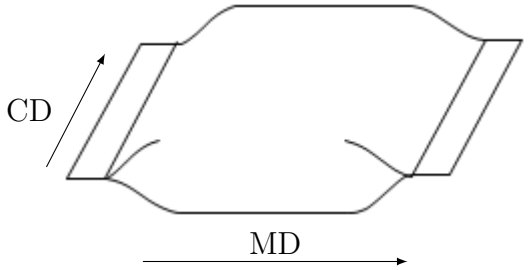

Figure 5.16: Definition of machine direction (MD) and cross machine direction (CD) of a package.

The aluminium foil and its adhesives, as well as the inner polymer layer are closest to the fluid inside of the package. Hence, a rupture will appear only when these layers have first fractured. Therefore, results of stresses and strains are only shown for these plies. Figures of stresses and strains are taken at a top plate reaction force of 1498 N, i.e. the average failure load of the physical tests.

Values of the stresses are shown using quilt plotting, which means that the values, taken at the integration points of each element, are calculated as a weighted sum. In this manner, a single value for each element may be estimated.

5.3.5 Stresses in machine direction

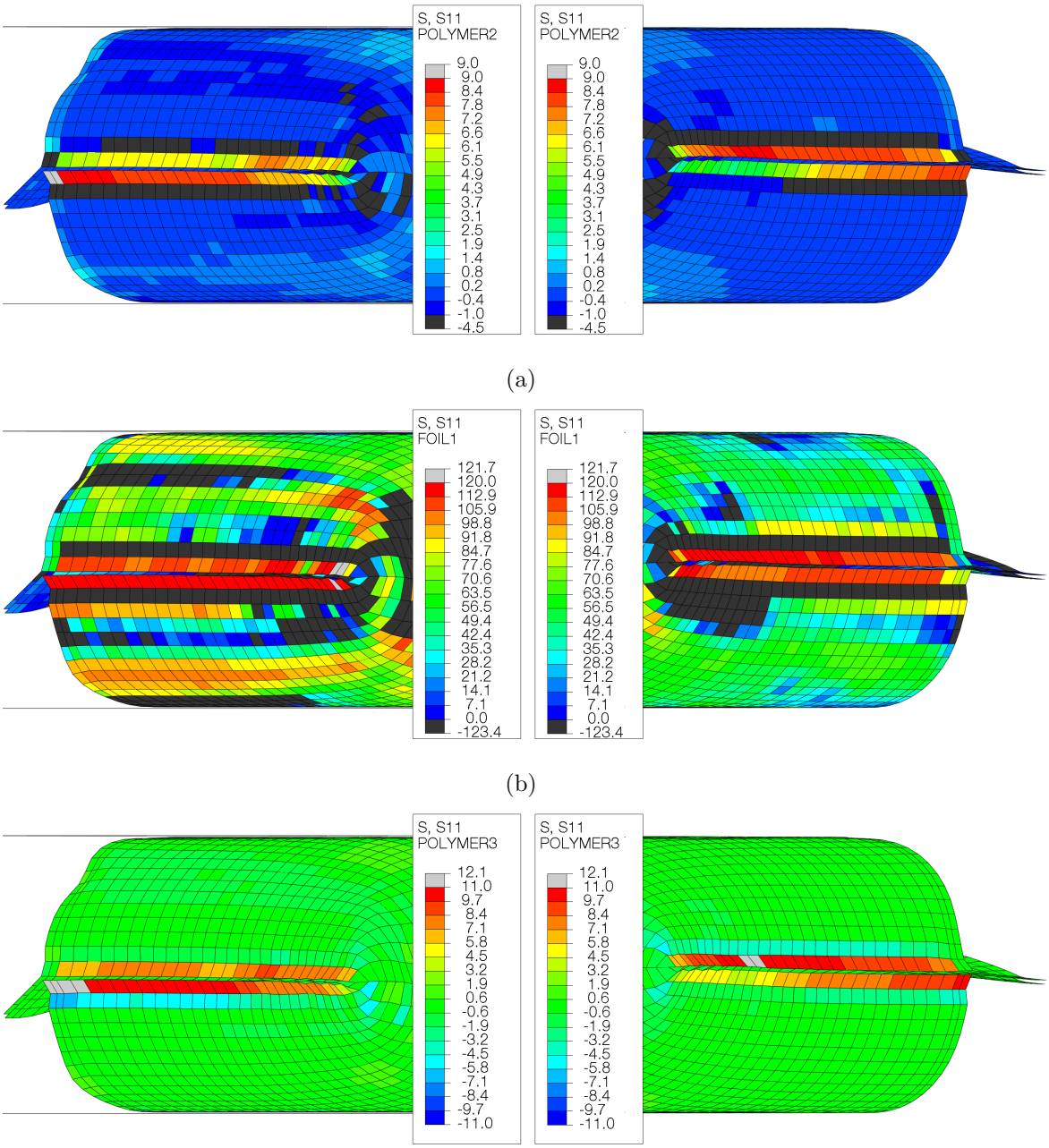

Figure 5.17: Stresses in machine direction for a) the adhesive (POLYMER2) b) the aluminium foil (FOIL1) and c) the adhesive (POLYMER3) for the top (left) and bottom (right) of the package [MPa].

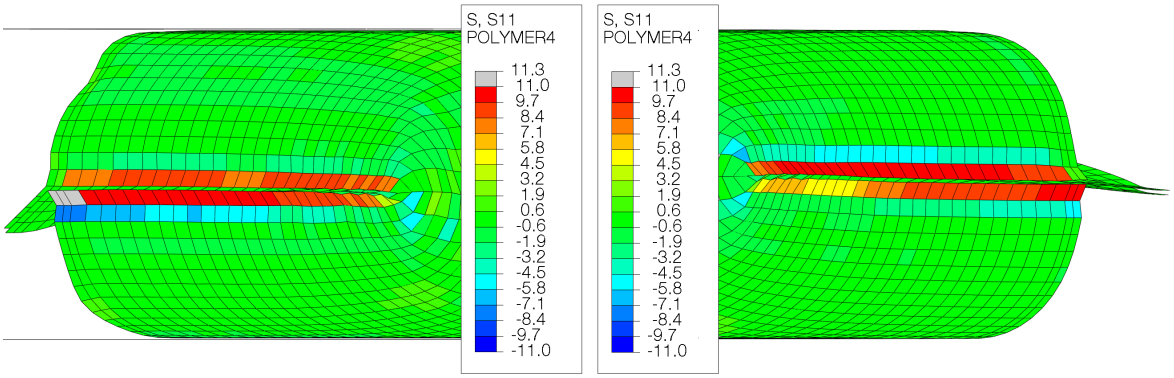

(d)

Figure 5.17 (Cont.): Stresses in machine direction for d) the inner layer (POLYMER4) for the top (left) and bottom (right) of the package [MPa].

5.3.6 Stresses in cross machine direction

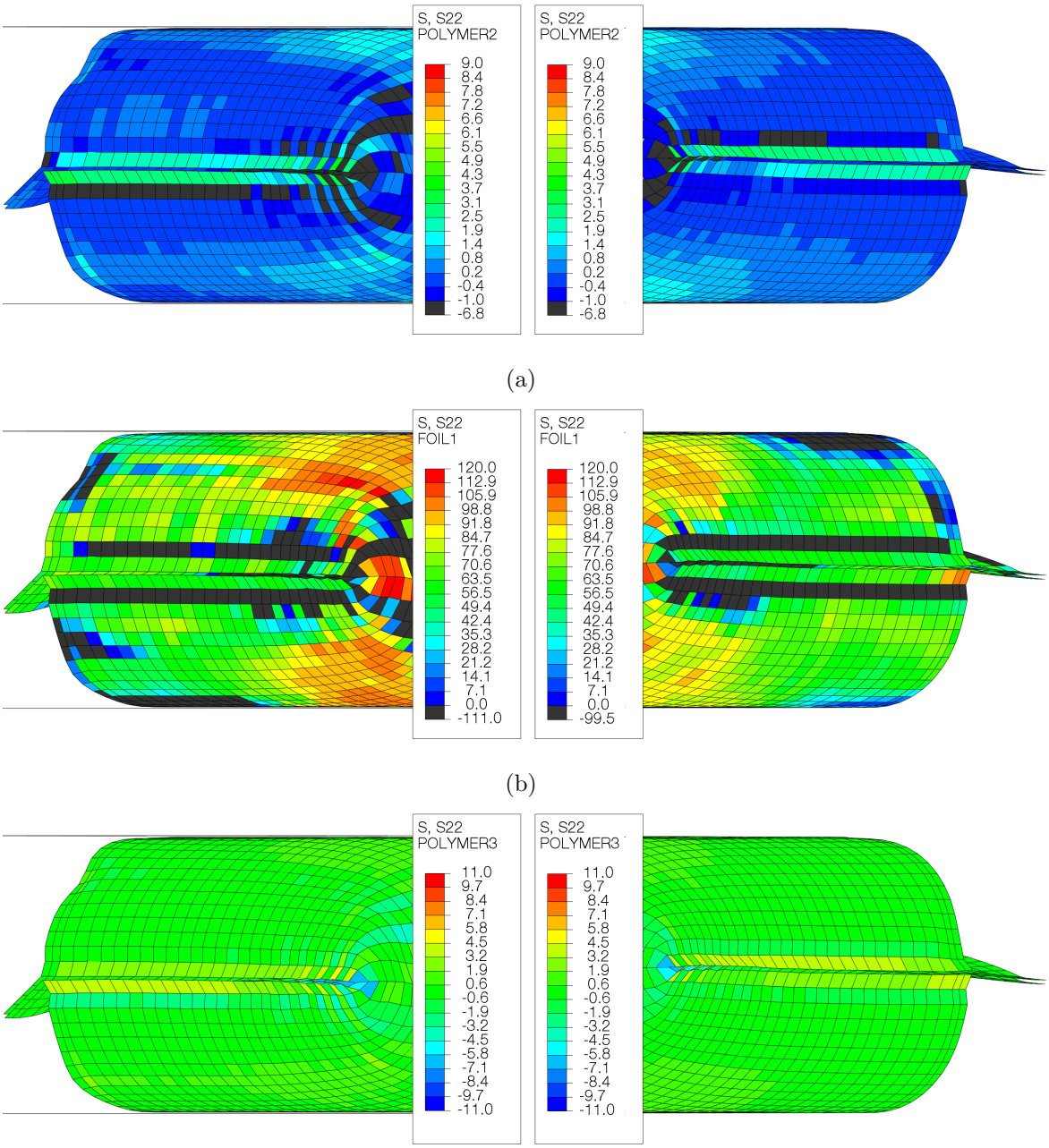

Figure 5.18: Stresses in cross machine direction for a) the adhesive (POLYMER2) b) the aluminium foil (FOIL1) and c) the adhesive (POLYMER3) for the top (left) and bottom (right) of the package [MPa].

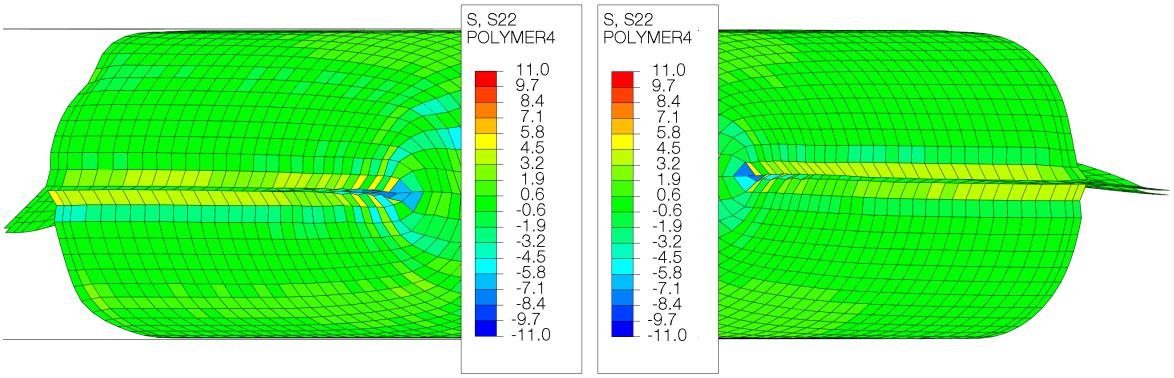

(d)

Figure 5.18 (Cont.): Stresses in cross machine direction for d) the inner layer (POLYMER4) for the top (left) and bottom (right) of the package [MPa].

5.3.7 Von Mises stresses

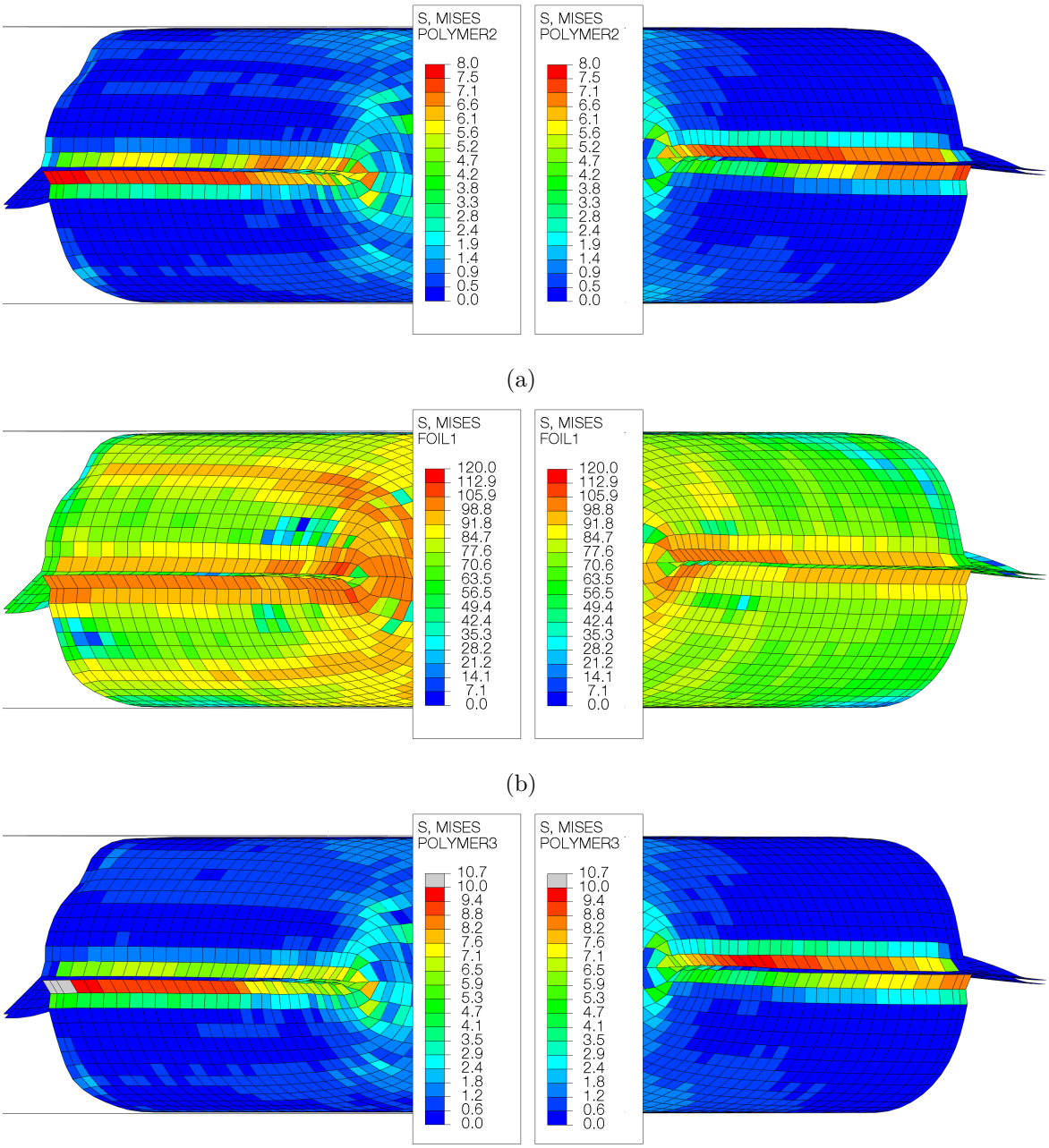

Figure 5.19: Von Mises equivalent stresses for a) the adhesive (POLYMER2) b) the aluminium foil (FOIL1) and c) the adhesive (POLYMER3) for the top (left) and bottom (right) of the package [MPa].

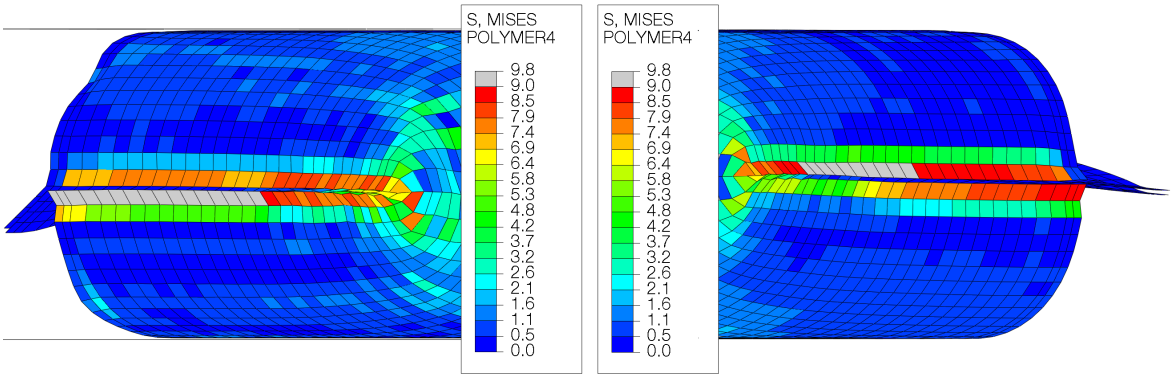

(d)

Figure 5.19 (Cont.): Von Mises equivalent stresses for d) the inner layer (POLYMER4) for the top (left) and bottom (right) of the package [MPa].

5.3.8 Plastic strains in machine direction

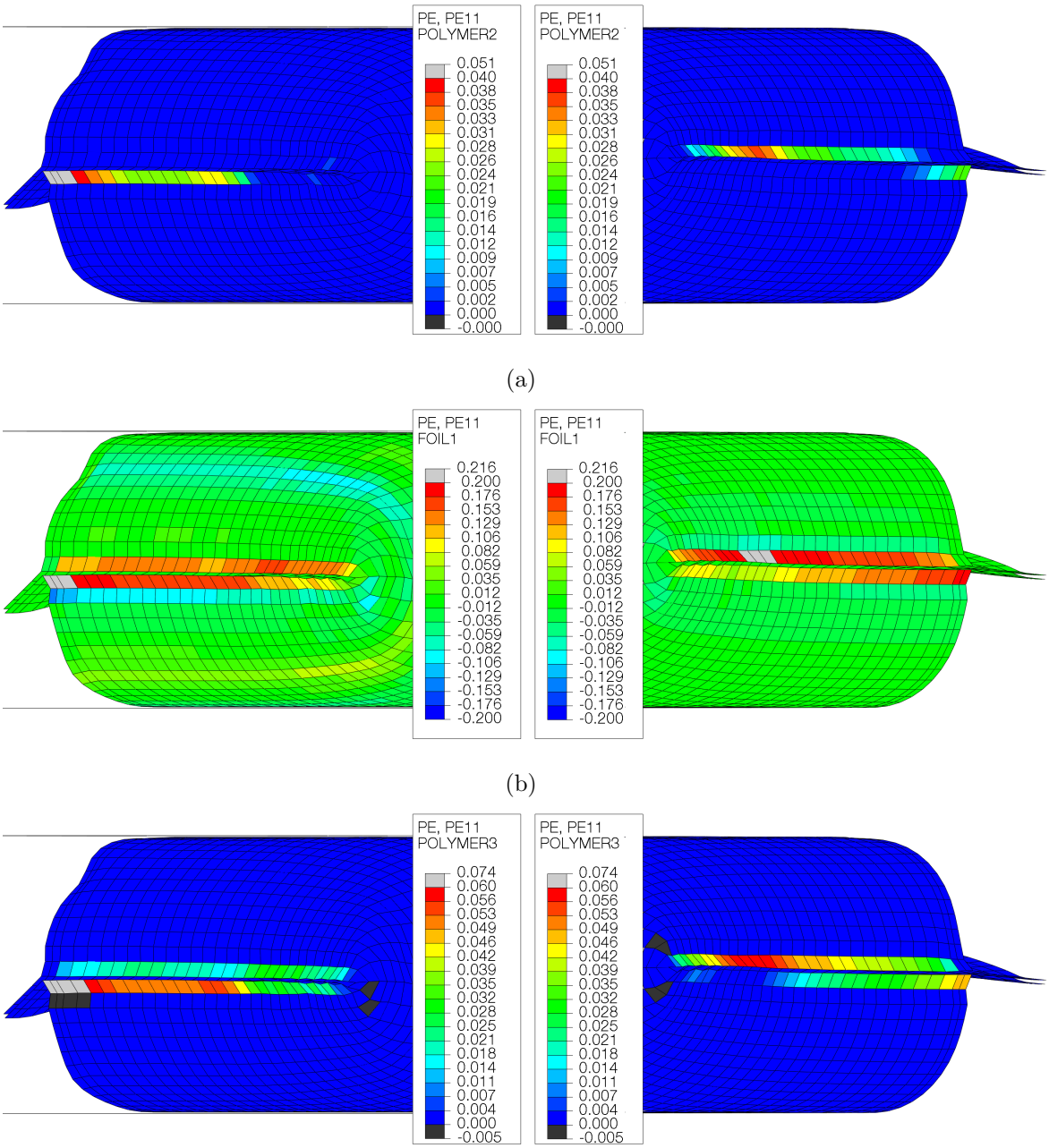

Figure 5.20: Plastic strains in machine direction for a) the adhesive (POLYMER2), b) the aluminium foil (FOIL1) and c) the adhesive (POLYMER3) for the top (left) and bottom (right) of the package [-].

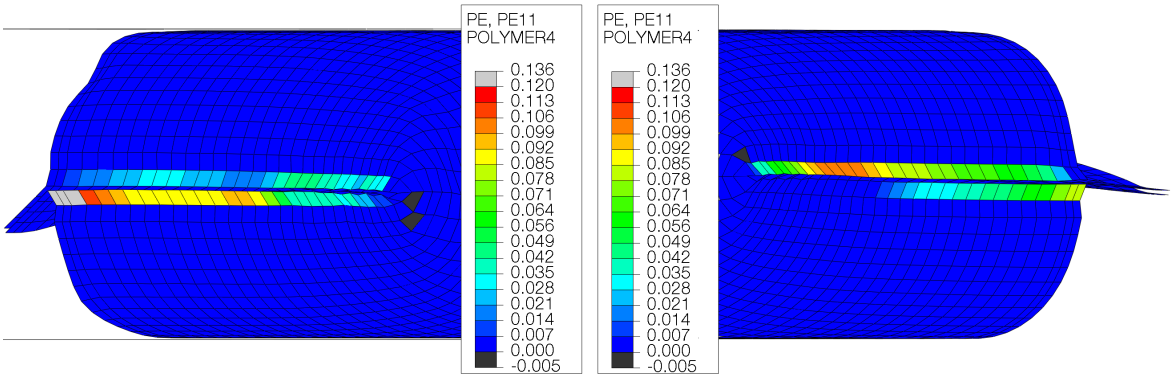

(d)

Figure 5.20 (Cont.): Plastic strains in machine direction for d) the inner layer (POLYMER4) for the top (left) and bottom (right) of the package [-].

5.3.9 Plastic strains in cross machine direction

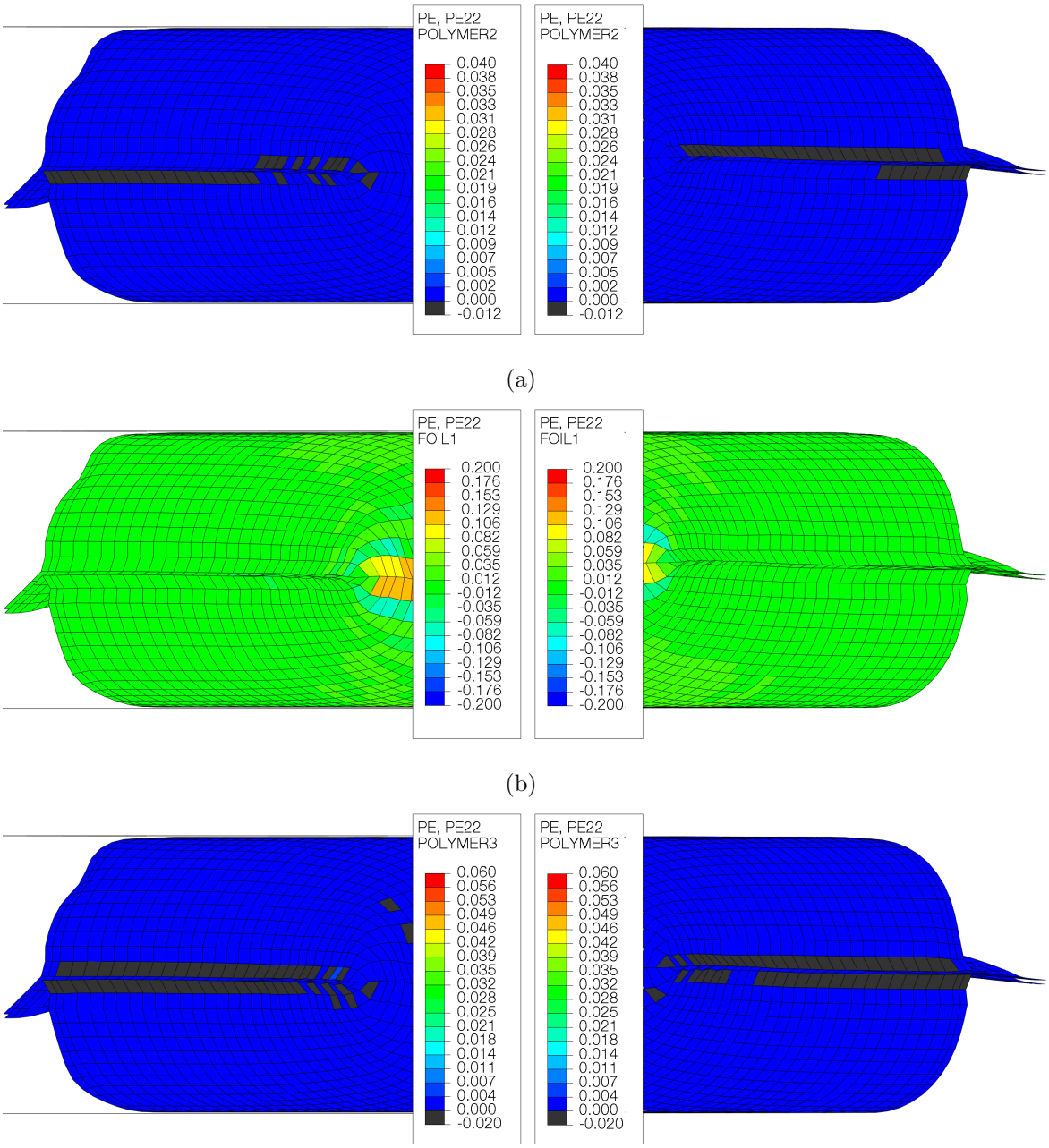

Figure 5.21: Plastic strains in cross machine direction for a) the adhesive (POLYMER2) b) the aluminium foil (FOIL1) and c) the adhesive (POLYMER3) for the top (left) and bottom (right) of the package [-].

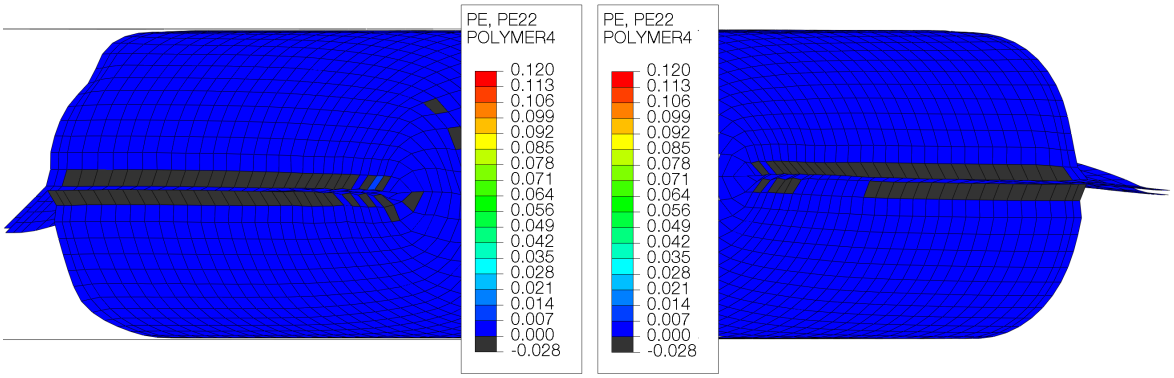

(d)

Figure 5.21 (Cont.): Plastic strains in cross machine direction for d) the inner layer (POLYMER4) for the top (left) and bottom (right) of the package [-].

5.3.10 Equivalent plastic strains

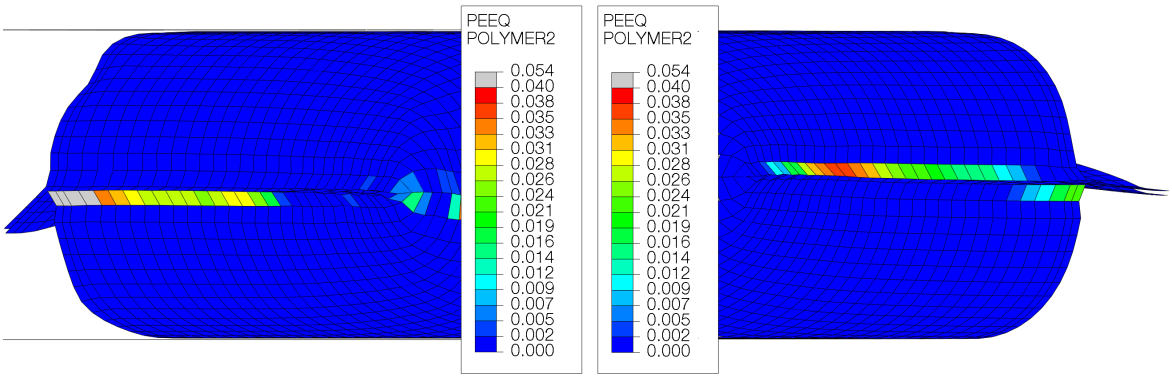

(a)

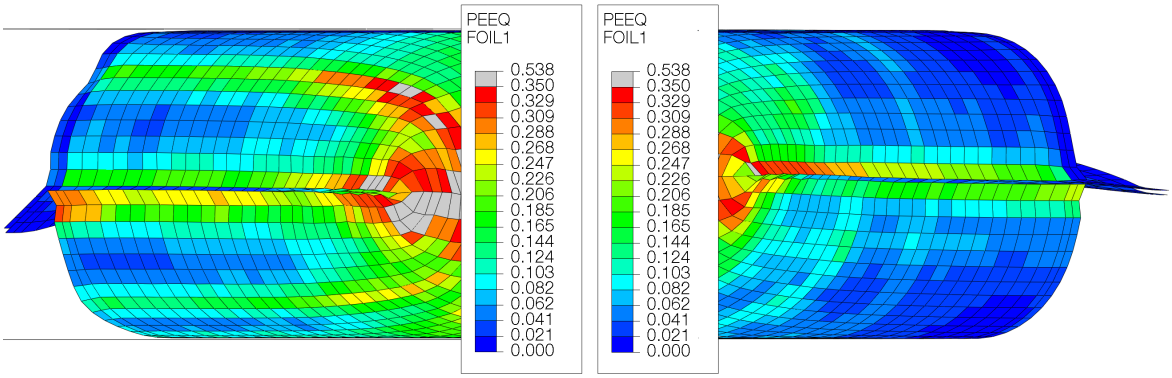

(b)

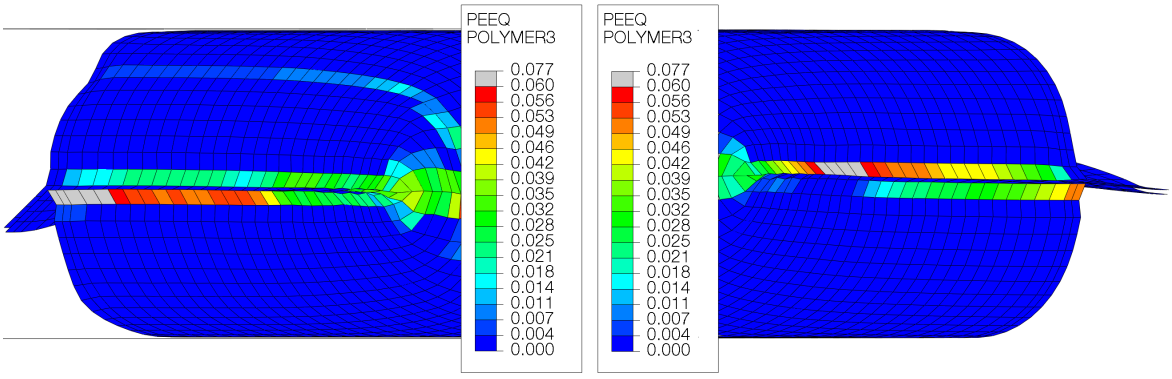

(c)

Figure 5.22: Equivalent plastic strains for a) the adhesive (POLYMER2) b) the aluminium foil (FOIL1) and c) the adhesive (POLYMER3) for the top (left) and bottom (right) of the package [-].

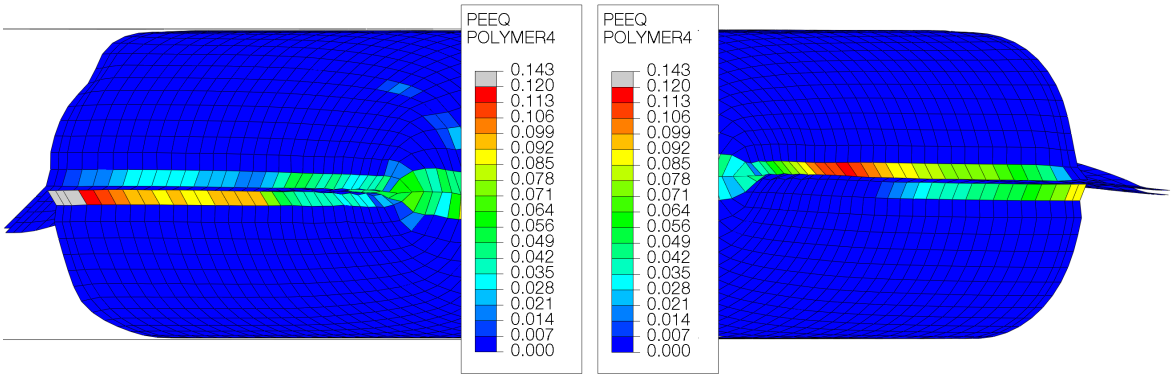

(d)

Figure 5.22 (Cont.): Equivalent plastic strains for d) the inner layer (POLYMER4) for the top (left) and bottom (right) of the package [-].

5.3.11 Energy

For the S4R element simulations artificial strain energy is present. This is not the case for the S4 element simulations. In Figure 5.23 artificial strain energy for the model using S4R elements, both directly and as a fraction, is compared to the total internal energy.

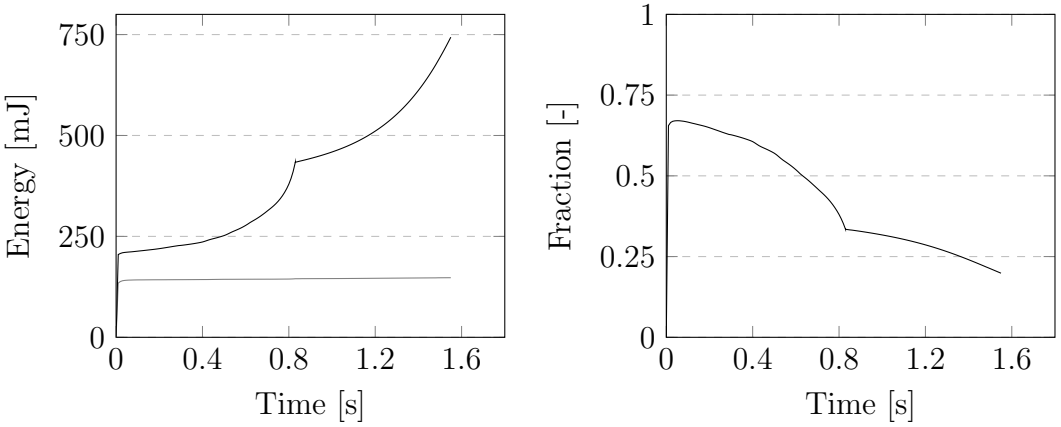

(a) (b)

Figure 5.23: a) Artificial strain energy (gray line) compared to total internal energy (black line). b) Artificial strain energy as a fraction of total internal energy.

5.4 Double package virtual compression tests

It was determined that the best parameters to compare in terms of stresses and strains between the different overlaps was von Mises equivalent stresses and equivalent plastic strains. Also, since the most critical layers are the foil and its adhesives, only these were included in the results of Section 5.4.4 and 5.4.5. Results in these sections are taken at a constant, specific load of 1500 N so that the material state may be compared directly between the different patterns.

5.4.1 Deformation

In the virtual case, only the deformation during compression may be shown. The model has no fracture mechanics, whereby images of a ruptured package cannot be obtained. The virtual deformations of the two packages P1 and P2 when using different overlaps are shown in Figure 5.24

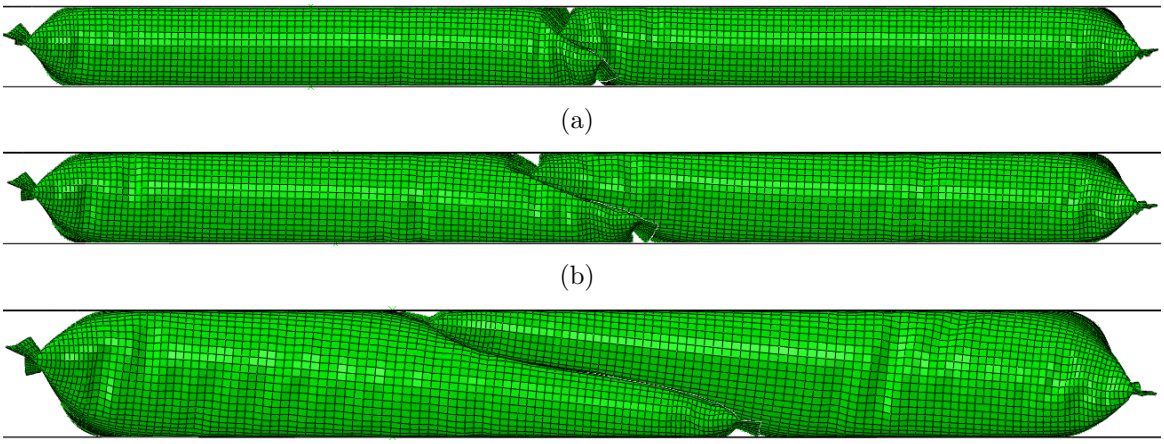

Figure 5.24: Deformation of packages P1 and P2 at a) 12.5%, b) 25% and c) 50% overlap.

5.4.2 Force-displacement data

Below, in Figure 5.25, calibrated average force-displacement curves from the physical tests are compared to corresponding force-displacement curves obtained from simulations. Simulation results are shown as solid lines, whereas average compression data is shown with dashed lines. Data for the three tested overlaps 12.5%, 25% and 50% is shown.

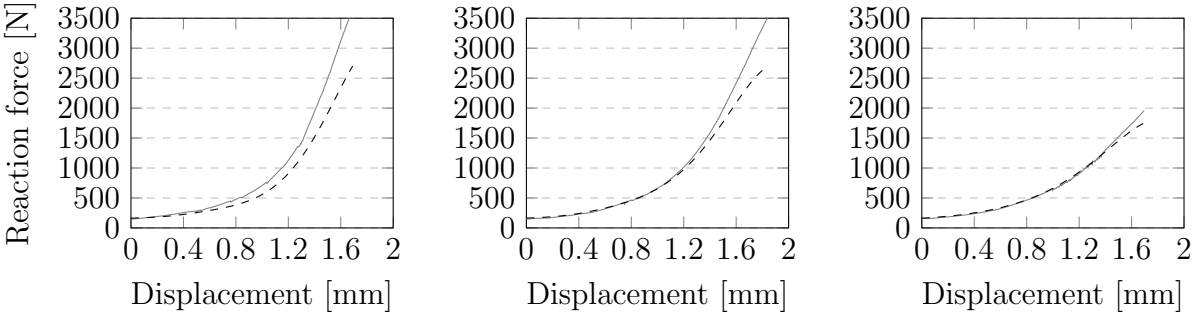

Figure 5.25: Average force-displacement curves compared to simulations for a) 12.5%, b) 25% and c) 50% overlap.

The force-displacement data from each of the simulations using different overlaps is shown as a comparison in Figure 5.26.

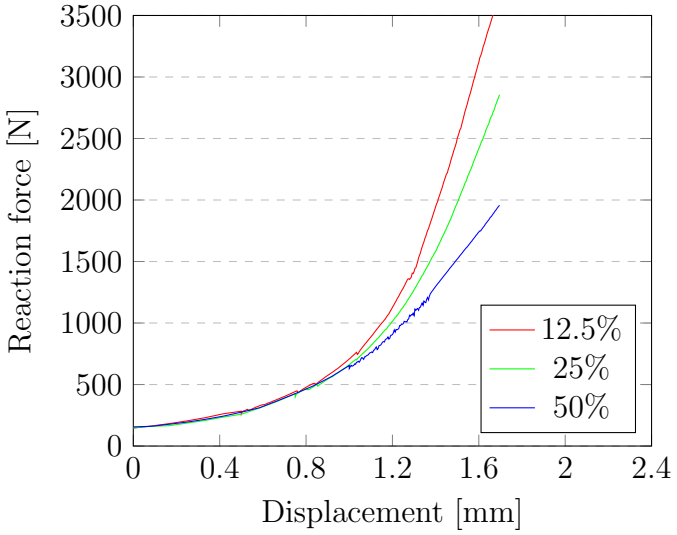

Figure 5.26: Calculated force-displacement curves for 12.5%, 25% and 50% overlap, respectively.

5.4.3 Pressure-force data

Internal pressures of P1 and P2 as a function of the top plate reaction force is shown in Figure 5.27 for different overlaps.

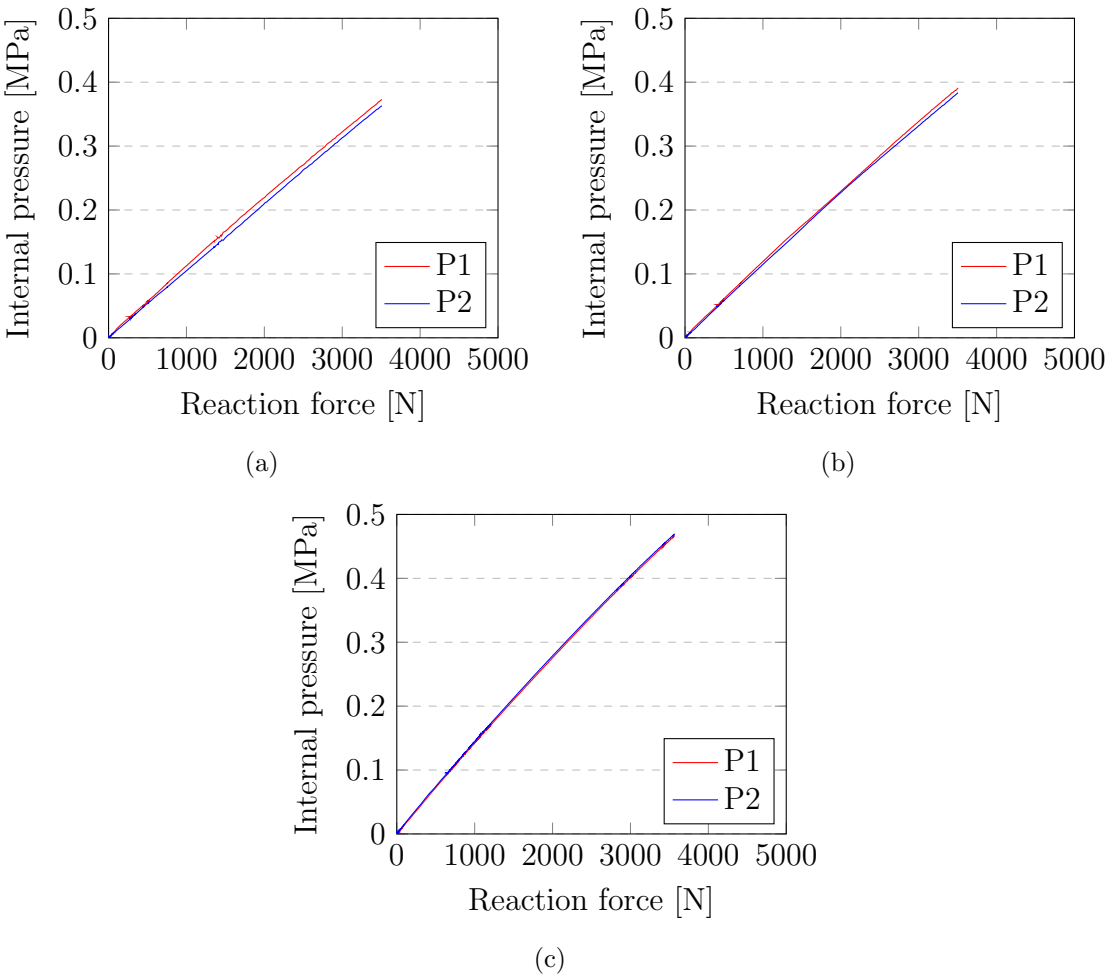

Figure 5.27: Internal pressure of the two packages P1 and P2 as a function of reaction force for a) 12.5% b) 25% and c) 50% overlap, respectively.

A comparison of the internal pressures of the different tested overlaps is shown in Figure 5.28. Here, the average values of package P1 and P2 have been used. Also shown is the pressure of the single package, as seen in Figure 5.14. Every value of the reaction force has been multiplied by a factor of 2 in order to estimate how the internal pressure would be if two packages were placed next to each other, i.e. if the force was to be distributed equally between the packages. This would correspond to a 0% overlap.

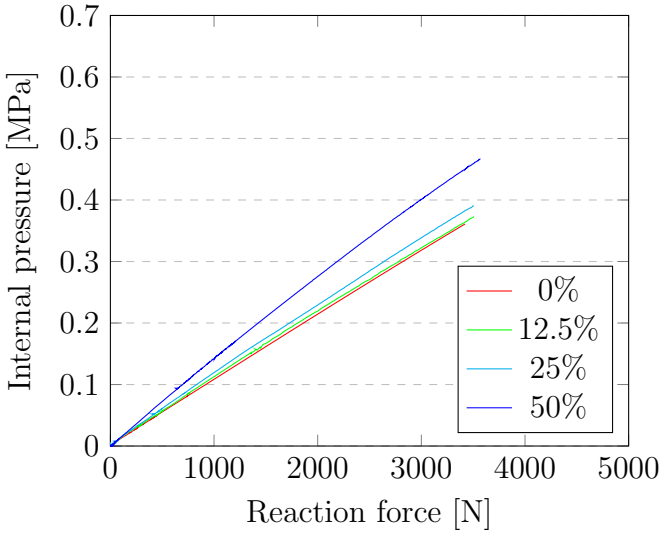

Figure 5.28: Internal pressure as a function of reaction force for 0%, 12.5%, 25% and 50% overlap, respectively.

Finally, the calculated internal pressures at failure load for each overlap, as well as for a single package, have been obtained and compared in Figure 5.29. The pressures for each overlap have also been taken at ±1.96 standard deviations, i.e. a 95% confidence interval assuming a normal distribution of package data. In this manner, an interval of the maximum and minimum expected rupture pressure may be included in Figure 5.29.

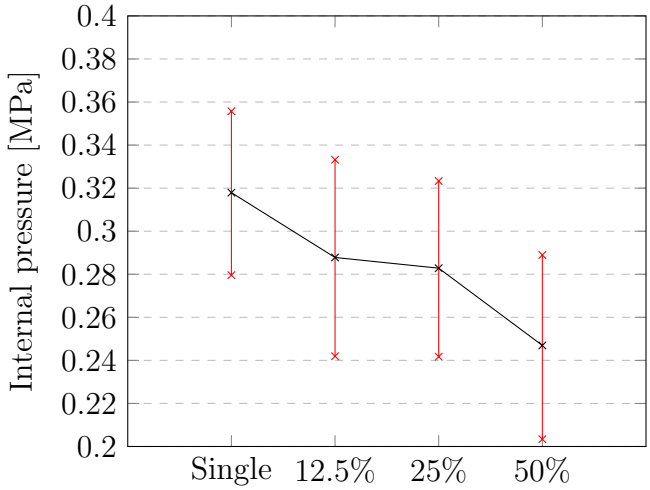

Figure 5.29: Internal pressure at the average rupture loads for each of the overlaps as well as the single package. A 95% confidence interval for each pattern is also shown in red.

5.4.4 Von Mises stresses

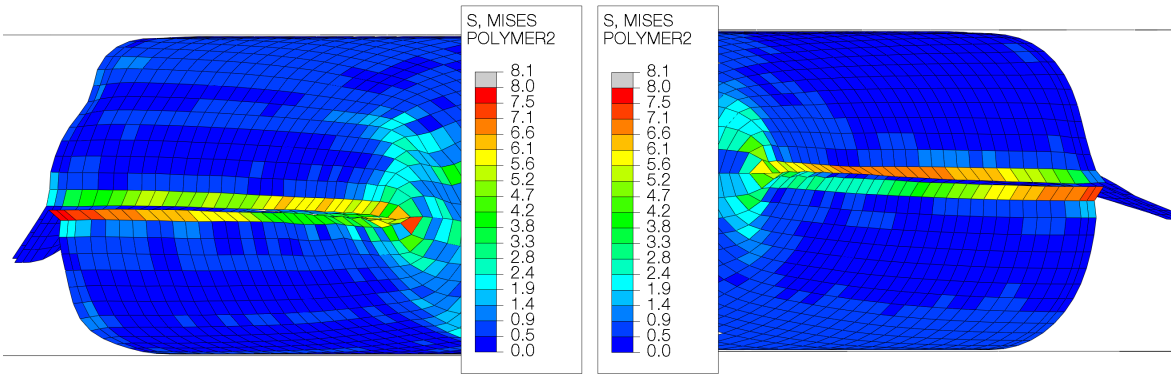

(a)

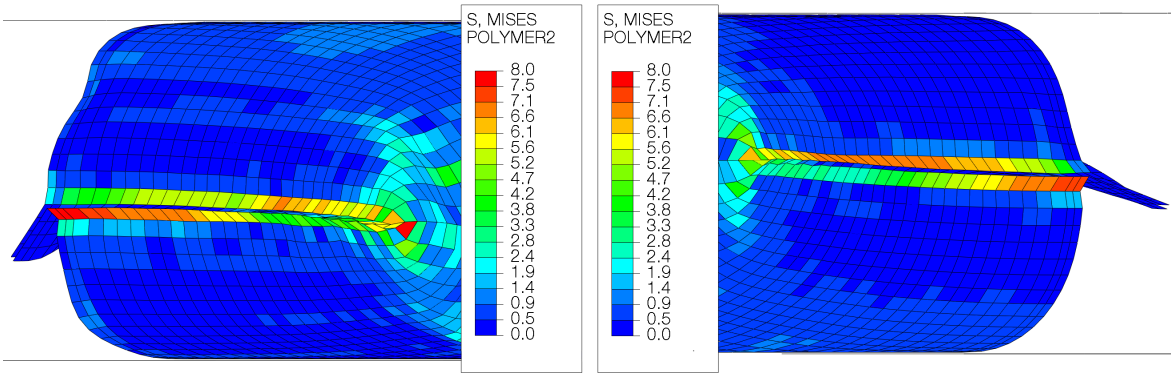

(b)

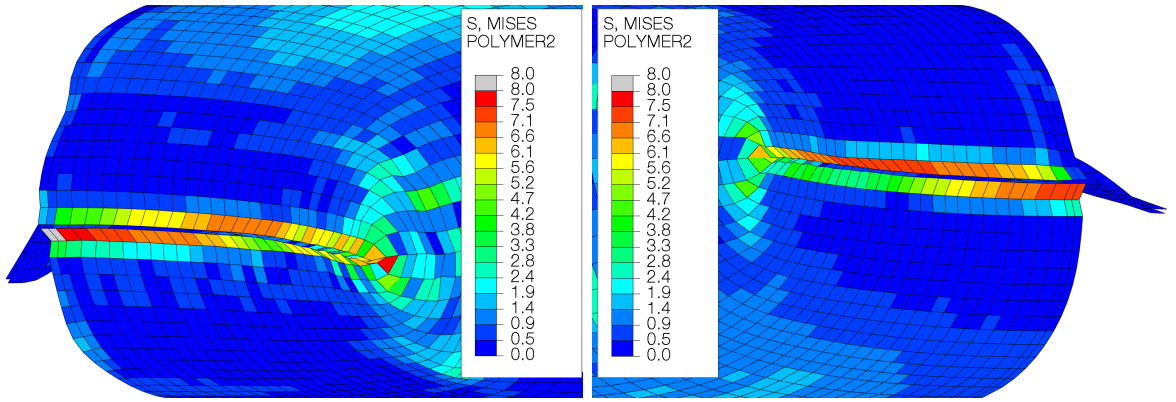

(c)

Figure 5.30: Von Mises equivalent stresses in polymer 2 for the top of package P2 and bottom of package P1 for a) 12.5% b) 25% and c) 50% [MPa].

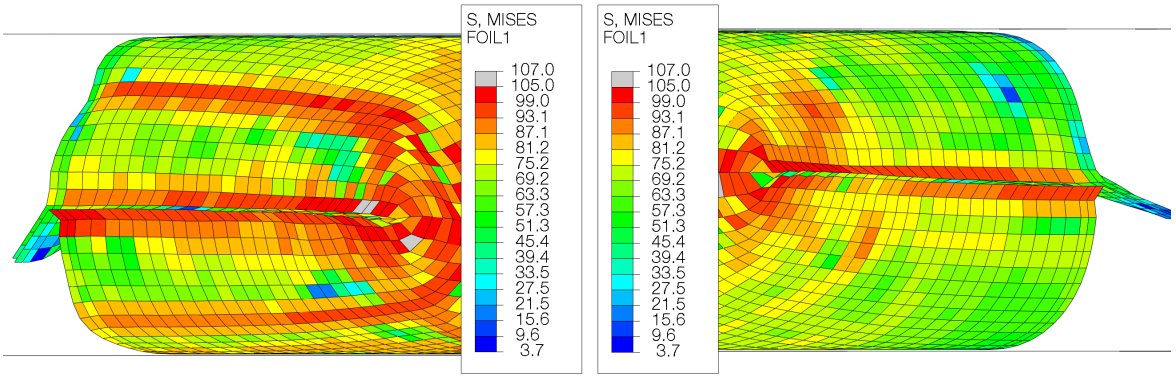

(a)

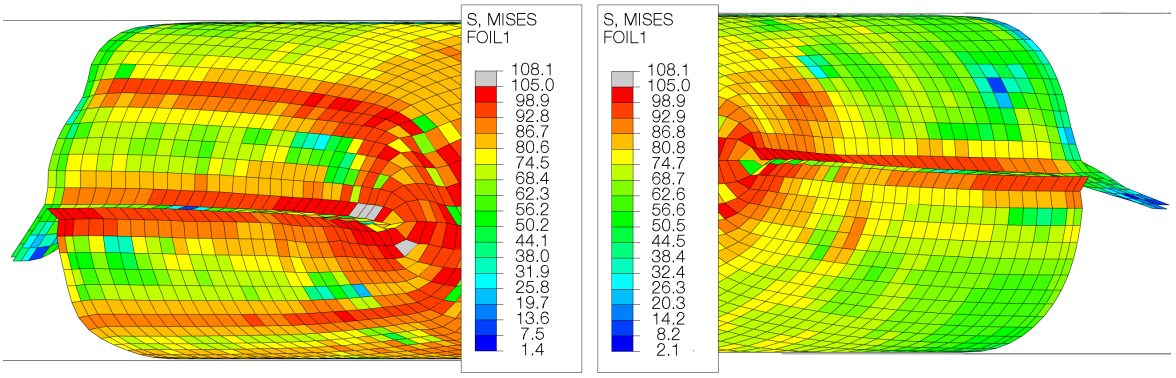

(b)

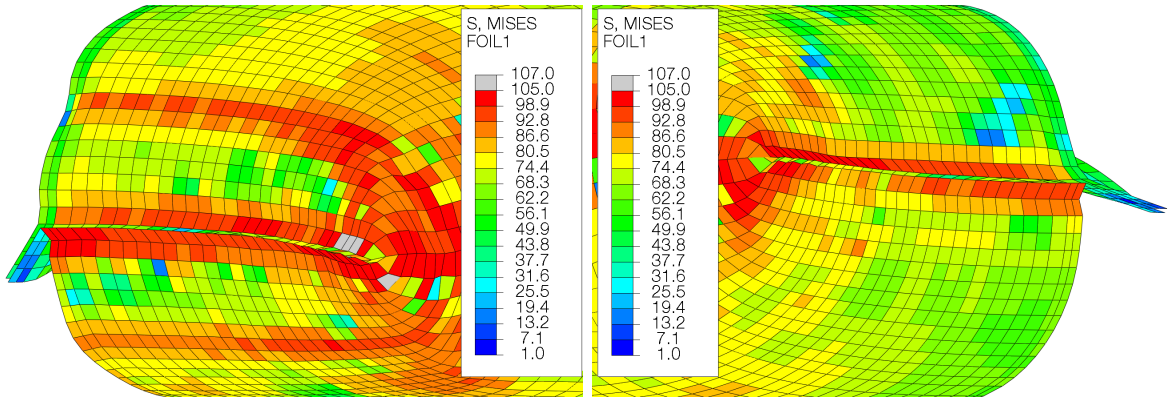

(c)

Figure 5.31: Von Mises equivalent stresses in the aluminium foil for the top of package P2 and bottom of package P1 for a) 12.5% b) 25% and c) 50% [MPa].

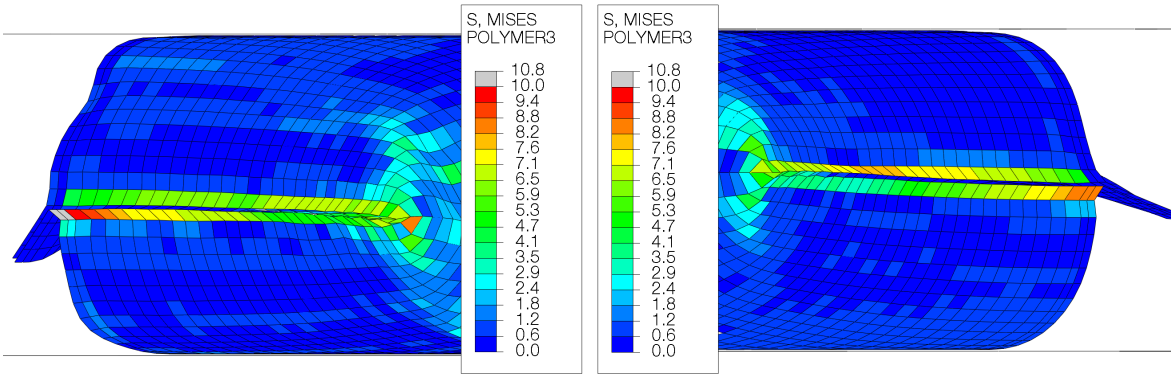

(a)

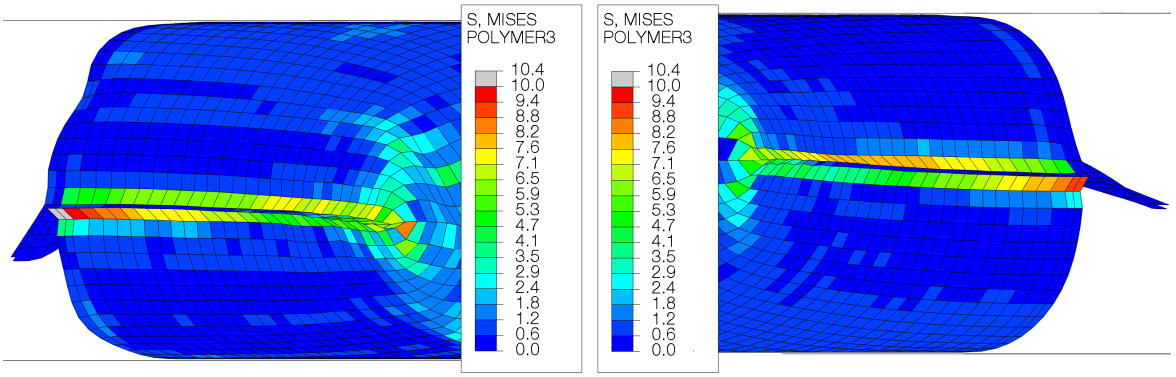

(b)

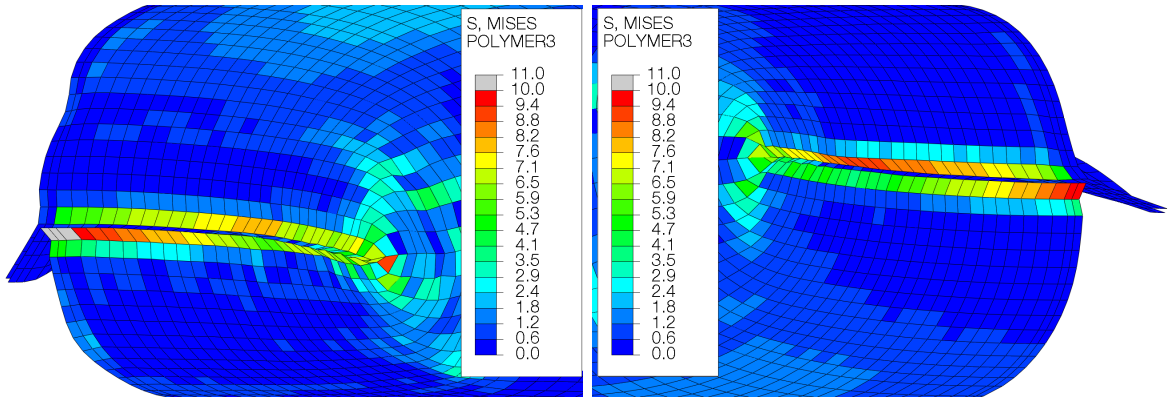

(c)

Figure 5.32: Von Mises equivalent stresses in polymer 3 for the top of package P2 and bottom of package P1 for a) 12.5% b) 25% and c) 50% overlap [MPa].

5.4.5 Equivalent plastic strains

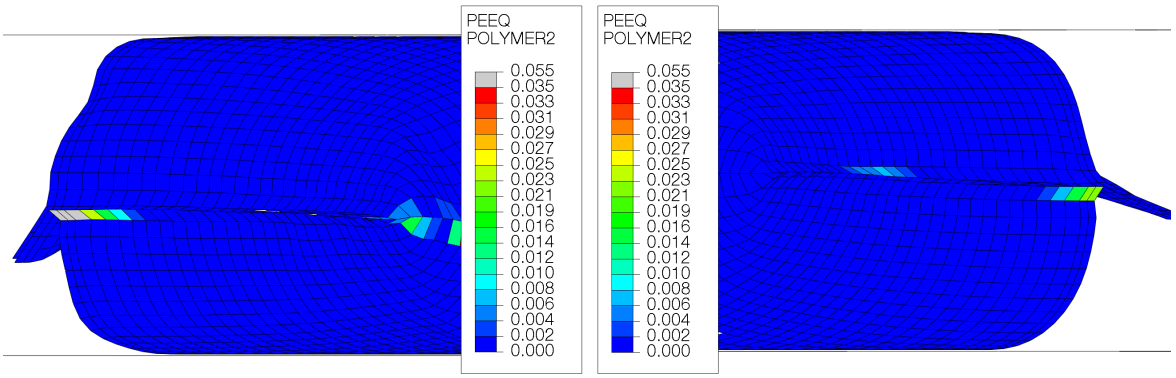

(a)

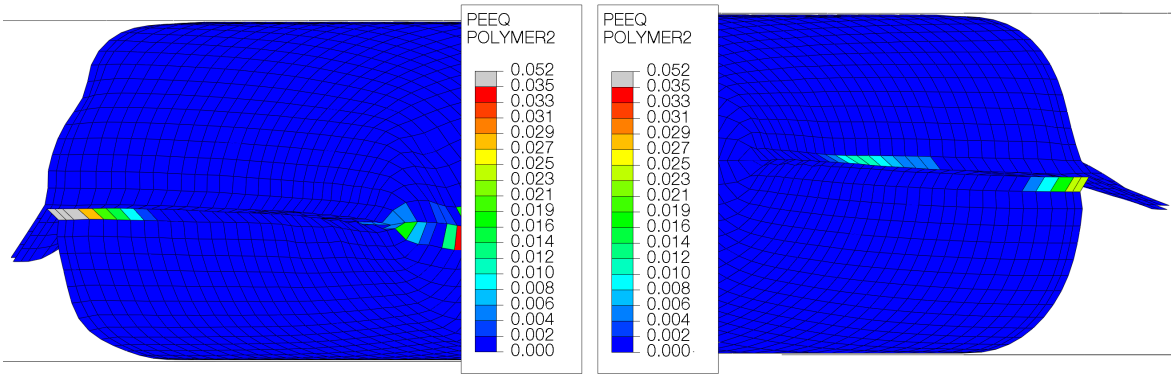

(b)

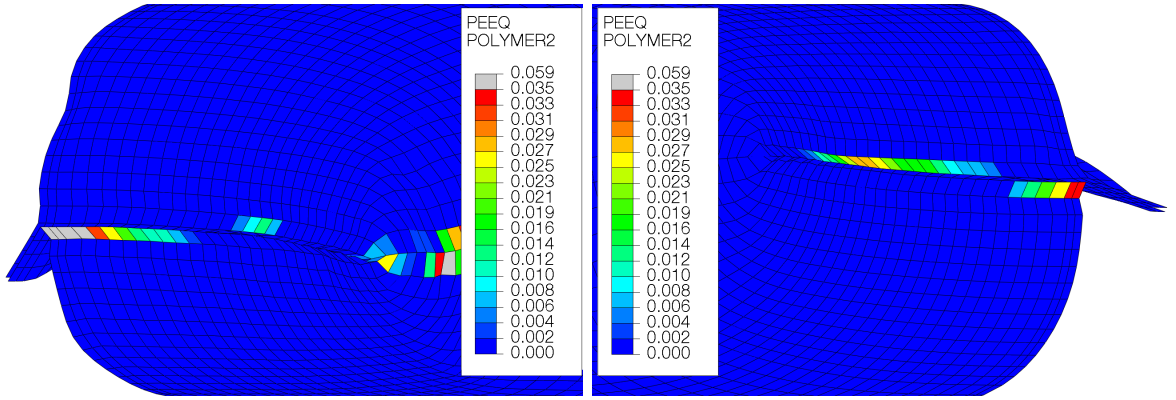

(c)

Figure 5.33: Von Mises equivalent stresses in polymer 2 for the top of package P2 and bottom of package P1 for a) 12.5% b) 25% and c) 50% [MPa].

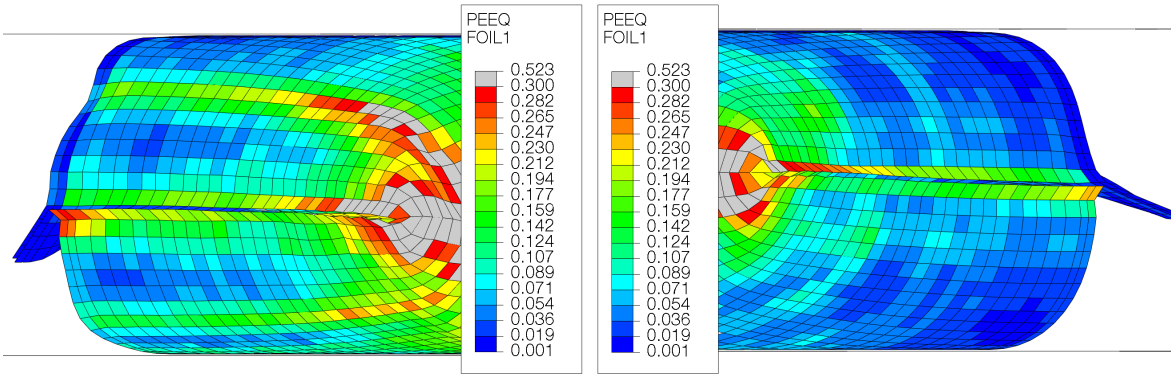

(a)

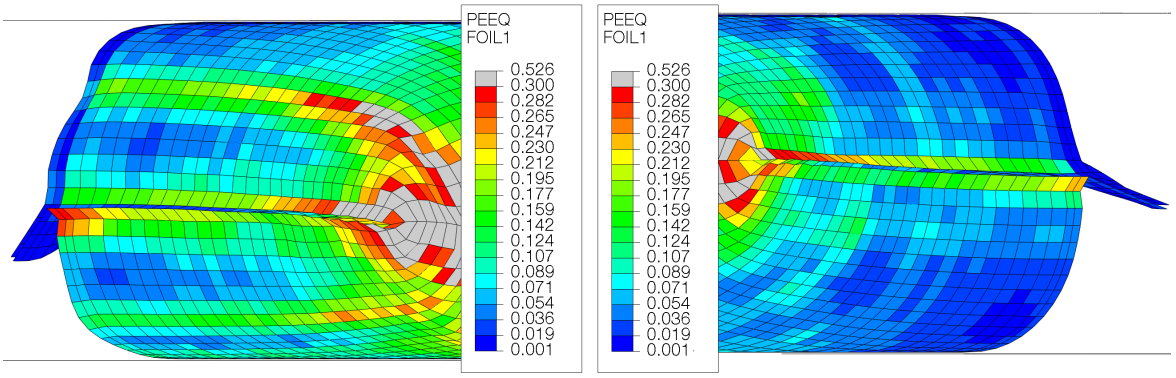

(b)

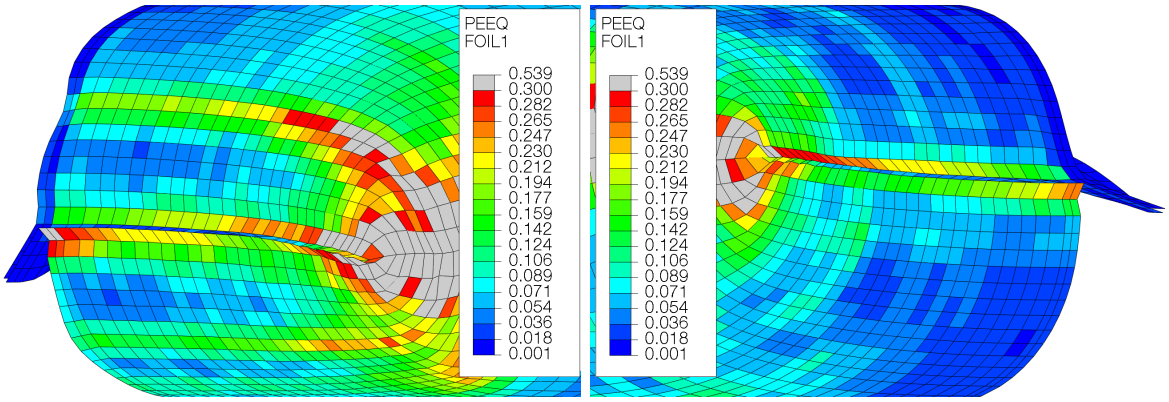

(c)

Figure 5.34: Equivalent plastic strains in the aluminium foil for the top of package P2 bottom of package P1 for a) 12.5% b) 25% and c) 50% [-].

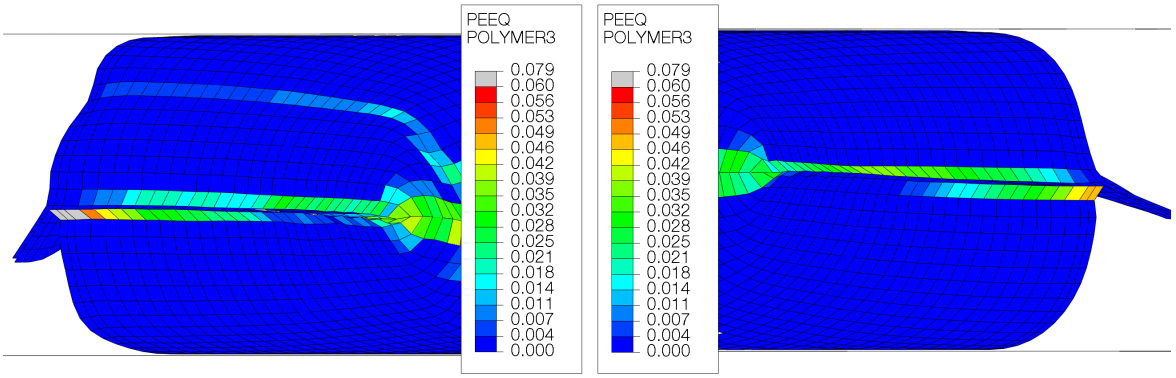

(a)

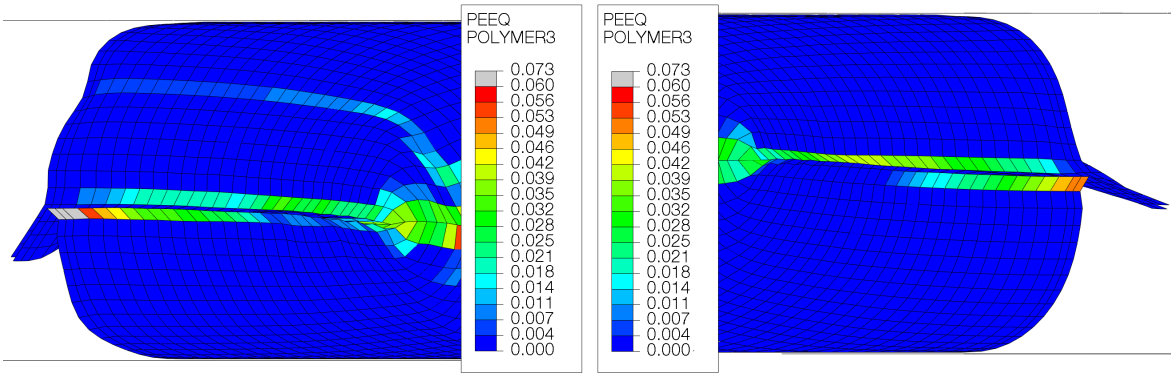

(b)

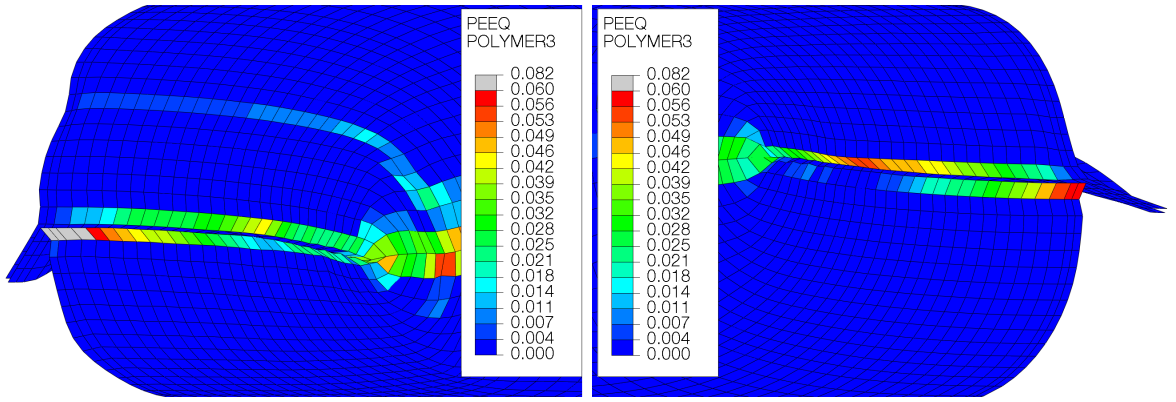

(c)

Figure 5.35: Equivalent plastic strains in polymer 3 for the top of package P2 and bottom of package P1 for a) 12.5% b) 25% and c) 50% overlap [-].

5.5 Package stacking virtual compression tests

Due to limited amount of packages and time, no physical tests were conducted for the package stacking. Stresses and strains are not included either, as only the macroscopic behaviour is relevant.

5.5.1 Force-displacement data

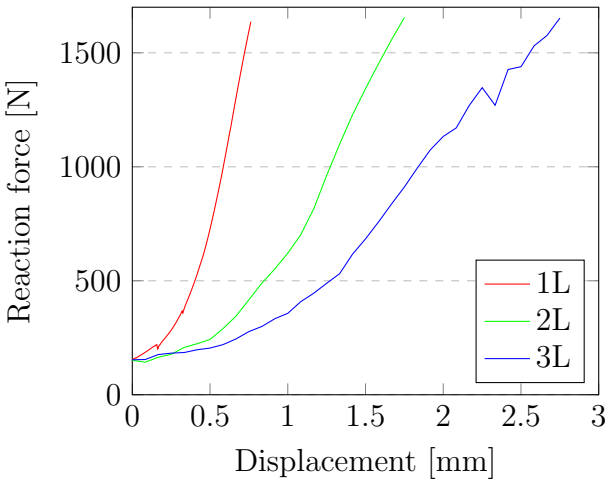

Figure 5.36: Calculated force-displacement curves force for one, two and three package layers (1L, 2L and 3L).

5.5.2 Pressure-force data

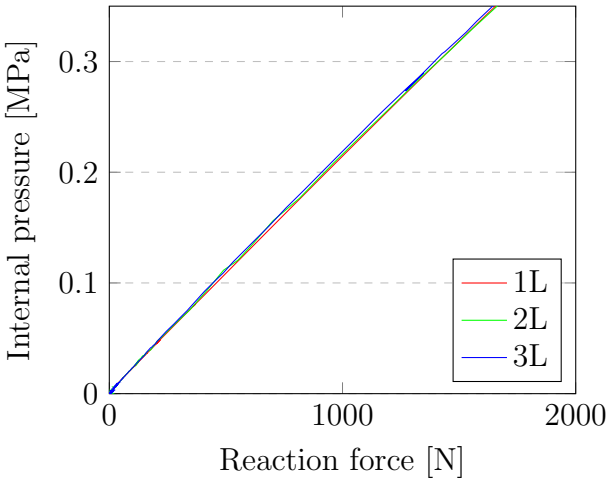

Figure 5.37: Internal pressure as a function of reaction force for one, two and three package layers (1L, 2L and 3L).

CHAPTER 6

Discussion

6.1 Single package physical compression tests

Rupture of a package subjected to a compression test is shown in Figure 5.2 and 5.3. It may be seen in Figure 5.3 that the fracture is present at the frontside, which is separated from the backside. It is located, as indicated in Section 1.3 close to the seal, while the seal itself is still intact. The outer layer of the frontside does not have a tear, so there must have been a delamination in the material. Most likely, the paperboard has separated, perhaps from it being soaked.

By studying Table 5.1 and 5.2, it may be noted that the average failure load is about 1500 N, and that the most common rupture position is frontside bottom. A standard deviation of 95 N corresponds to about 6% spread from the average value. Hence, the failure load may be fairly well estimated by the average value.

From Figure 5.4 it may also be seen that the individual test data follows roughly the same path. The maximum span is about 250 N. Also both the failure load and failure displacements vary somewhat. The reasons for these variations is the randomness of the package forming process, making the packages slightly different in size and shape, with various wrinkles.

A source of error that may or may not be relevant is that the top plate had to be aligned to the bottom plate manually. Even though they were brought completely

together during aligning, there might still be some non-parallelity causing a biased failure position. For example, should the top plate be tilted slightly to the right, most likely a larger load will appear on this side. Hence, the rupture positions shown in Table 5.2 may be biased.

A more accurate distribution would be obtained if more packages were tested. This would however be too time consuming and in the end not relevant for the purpose of this thesis.

6.2 Double package physical compression tests

By studying Table 5.3, it may be noted that the average failure load is increased from about 1750 N for 50% overlap to 2750 N for 12.5% overlap. Hence, the average failure load seem to increase with decreasing overlap. The most likely explanation is that the plate force is distributed on a larger surface. Standard deviations of the tests lie in the range of about 8-10%, which regarding variations of both package shape and placement is quite small.

From Table 5.4 it is clear that the bottom package P1 ruptured in the majority of the tests, and at the same position, frontside bottom, as well. The fracture itself looks like that found in the single package test. The reason for having the same rupture position for the majority of the tests is not found easily. However, some theories may be presented.

It may be a dent in the top of the packages, introduced on purpose in the forming process as a way of adjusting package length, which stretches the material. By doing so, permanent deformations arise that will probably have some residual stresses. These, in turn, may prevent large deformations and high stresses from arising close to the seals. This may make the difference on which side of the package that ruptures. Otherwise it may be some other effect of forming that instead weakens the bottom.

It may also be that the top plate of the test equipment is misaligned, thus causing a biased result. However, some additional tests, outside of the test series, where the packages were placed in the opposite direction were conducted, where every single test had a rupture at P1 frontside bottom. Hence, this misalignment is less likely than the reason stated in the previous paragraph.

Something else worth noticing is that none of the packages ruptured in the overlap zone. The probable reason for this is that the packages will support each other, and put pressure on the individual package ends hence reducing the possibility of tensile stresses to develop inside the package.

As in the case of the single package, a more accurate result would be obtained if more packages were tested. Other sources of error is that it was cumbersome to position

the packages perfectly with the correct overlap and in the same way every time.

Studying Figure 5.11, it is possible to see that the curves follow each other quite well to about 1.6 mm displacement. After that the curves separate and shown different stiffnesses. From this point it may be seen that the 12.5% overlap in general may take higher loads for a particular displacement. This suggests that this is a more robust configuration. The exception is between about 0.4 and 1.5 mm displacement, where it seems like the 12.5% overlap has a dip in its stiffness. This may be due to the fact that some minor sliding between the packages is occurring in this interval.

6.3 Single package virtual compression tests

It is seen in Figure 5.13 that the virtual test data using S4 elements follows the average test data quite well. Even though the curve does not follow the curve exactly, it should be considered that this is only an average data curve. If the spread seen in Figure 5.4 also included, it may be concluded that the virtual data lies well inside this spread zone. The curve of the S4R elements is also quite accurate, especially initially, but it seems to be more divergent at larger displacements. Hence, S4 elements are considered to be most suited in this case.

Something that is strange is that the S4R elements provide a stiffer solution than the S4 elements. This opposes the theory, c.f. Section 2.10, which states that full integration should provide a stiffer solution than reduced integration. The explanation is probably found by studying Figure 5.23. It may be seen that the artificial strain energy makes up a large portion of the total internal energy of the package, which indicates heavy hourglass controlling. It is possible that this extra internal energy will increase the stiffness of the structure. Most of this energy comes from the forming model as it may be seen that the artificial strain energy remains almost constant in the compression test. Hence, care was taken for the forming model which was changed into using S4 elements as well.

Tests using a finer mesh is also shown in Figure 5.13. These results are quite far from the average values, and the package did not behave as it should in the simulation either. The most likely reason for these errors is that the mass scaling had to be set too large, and the simulation time had to be reduced to an extent where dynamic effects are present. All in all, this lead to that the fine mesh was not used further.

Next, the stress and strain distributions in Figure 5.17-5.22 may be studied. Both the maximum stresses and strains appear at the positions where the package ruptures in the physical testing, namely near the TS. It is apparent that tensile stresses are dominant at the failure loads, as expected. Some stress concentrations may be present at other locations, especially at wrinkles, but may be neglected as it is known from testing that it is not a failure position. It is difficult, though, to tell anything about

exactly which side that will rupture and at which location. This is due to the fact that both stresses and strains are quite high along the entire seal.

The actual values when comparing e.g. machine direction stresses to material fracture data obtained previously at Tetra Pak differ. The strains in machine direction are also quite far from physical data. This makes it difficult to find a particular indicator or criterion to specify fracture. One of the reasons for having high stresses could be that delamination is not taken into consideration. Hence, the stiffest material, being the aluminium foil, will be more stressed than it would be if only aluminium was used. Especially, since the paperboard is the thickest ply it will also be the most dominating in the composite. Thus the total strains will also be the most affected by the paperboard stiffness which is lower than the foil stiffness.

By comparing stress results between Section 5.3.5 and 5.3.6 as well as strain results between Section 5.3.8 and 5.3.9, it may be concluded that the quantities in machine direction are greater than the cross machine direction quantities. By this it is indicated that the axial stress of the package is the cause of failure rather than the circumferential. Hence, the plausibility that the load situation for a compression test is similar to that of a wedge test is further increased.

The consequence of not using a proper fluid model inside cavity is that the package will not spread out properly due to gravity, and that the loads on the package due to the fluid will be omitted. However, under compression the pressure in the cavity will greatly exceed the hydrostatic pressure due to gravity. In order to show this, assume that the pressure at height z in the package is given by

$$p(z) = p_0 + \rho g z$$

where ρ is the fluid density and g the gravitational acceleration. The maximum pressure due to gravity is hence obtained by $p_{g,max} = \rho g z_{max}$. If the largest height z_{max} is taken as the nominal package height $h = 25\ mm$ the maximum pressure will approximately be

$$p_{g,max} = \rho g z_{max} \approx 1000 \cdot 9.81 \cdot 0.025 = 245.25\ Pa$$

This should be compared to a maximum cavity pressure of 0.32 MPa, as seen in Figure 5.14. The conclusion is that the hydrostatic pressure due to gravity is clearly negligible.

6.4 Double package virtual compression tests

Figure 5.25 shows that simulated data compares well to average physical test data for the double package tests. The exception is the 12.5% which is slightly more different

from test data. However, simulation data is still well inside the area of spread from testing.

Simulation data in Figure 5.26 also show that the stiffest solution is provided by the 12.5% overlap. It does not seem like the dip that is seen in the physical testing in Figure 5.11 is present though.

From Figure 5.27 it may be seen that the internal pressures are almost the same for the two packages. Something that may be worth to consider though is that the package with slightly higher pressure, P1, is also the package that is the most common to break in the physical testing. The difference in pressure seems to disappear when the overlap is increased, as may be seen by comparing c) to a).

Next, turning to Figure 5.28 it is clear that the internal pressure at a certain load is increased with increasing overlap. This could be due to the fact that the load from the top plate is distributed on a larger surface when the overlap is decreased. From the same figure, internal pressures using overlap may be compared to internal pressure without any overlap. It seems like 0% overlap has almost the same result as 12.5% overlap. Hence, there should be no advantage in removing the overlap in order to potentially increase the total load-taking surface. An argument for not using 0% overlap though is that this will expose the P1 top and P2 bottom ends of the two packages, hence increasing the probability of a rupture.

A question that arises is whether the internal pressure alone may determine a state at which the package ruptures. A comparison of the different simulated pressures at the respective failure loads, including the failure load variations, may be seen in Figure 5.29. Using a 95% confidence interval, an indication of that the pressure at failure load decreases with increasing overlap may be seen. Hence, the internal pressure may not by itself be used to indicate failure. On the other hand, it may be stated that the pressure at rupture should lie somewhere in the range of 0.2-0.36 MPa.

As the previous paragraph suggests, something else than the internal pressure must affect the failure load. When the packages are compressed, it might be the geometry of the packages themselves that is positioned in a way that makes them more sensitive to compressive loads.

Looking at stresses and strains for two packages, clear differences may be seen for the different overlaps. Studying e.g. Figure 5.30 and 5.33 it may be seen that both equivalent stresses and strains increase with an increased overlap. The same trend may be seen for all plies. This means that both the internal pressure as well as stresses and strains indicate that more overlap causes higher loads on the package.

6.5 Package stacking virtual compression tests

If Figure 5.37 is studied, it may be seen that there is no major difference between the internal pressure curves of three layers and one layer. This is not strange since the plate will exert a force on the first package, which is then transmitted down to the bottom plate. If a free body diagram was to be drawn of the stacked packages, it would show that the force acting on each package would be the same. Hence, since the area on which the force acts is almost the same for every package, there should theoretically be no major difference compared to the single package failure load.

However, it may still be noted that this probably will not be the case in reality, since in a statistical sense, it is worse to have more packages stacked. The reason for this is that the probability of including a weaker package is increased with an increased number of packages. Due to the fact that all packages should be exposed to the same force, it will thus be the weakest package setting the failure load. A slight indication of this phenomenon may be seen from previous tests in Figure 1.7.

Figure 5.36 shows large differences in stiffness for the different force-displacement curves. This is not strange, however, since if one package must be compressed a certain amount in order to achieve a certain load, two packages must individually both be compressed this amount to achieve this load. Are the packages then stacked on top of each other, the total compression to achieve a certain load must be twice of that that for a single package. For three stacked packages, the total compression must instead be three times more than for a single package. To further explain this, an analogy to elastic springs may be made. For a certain total displacement, one spring will have a larger force than two or three connected in a series. In other words, a comparison of force-displacement data is not entirely relevant.

6.6 Model limitations

When constructing a virtual model, it is usually not possible to take everything into consideration due to complexity and computational effort. The same applies in this case. The most difficult aspect to capture is the package forming randomness, i.e. that fact that no package looks perfectly alike. Small variations in speed, material orientation, timing etc. cause the packages to have minor differences. The exact trace of this phenomenon may not be found. More specifically, this means that real packages will not be completely symmetric, something that was assumed in the model.

Other aspects include the material state itself. It is assumed that the material will not be affected by anything other than stresses and strains. In reality, there may be some effect of temperature and humidity. Also, as the transversal and longitudinal seals are formed, the material is locally heated. From this there may be some effects. Moreover, the material models are time independent, so relaxation phenomena occurring is not

captured. Although the packages are mostly treated gently after leaving the filling machine, there may be effects of the after-treatment that is not included in the model. In the model, packages are taken straight from the machine.

As mentioned briefly in this thesis, the model fails to capture delamination, since the material is modeled as a composite shell. This is a limitation that will prevent a realistic material behaviour.

6.7 Conclusions

The first conclusion of this thesis is that it is only partially possible to compare virtual and physical data directly by means of the methods in this thesis. The overall behaviour of a package may be estimated by using a cavity interaction. However, when it comes to material quantities such as stresses and strains it may be concluded that the actual values at the expected rupture position are far from what is obtained from physical material data. Moreover, the microscopic fracture behaviour, described in Section 1.3, may not be captured by the current model. In order to perhaps be able to get an agreement of data, a much finer mesh density is required. This would however be extremely time consuming and hence not practical at the time being.

The second conclusion is that the overall behaviour of the packages may be used in order to compare different package shortside overlaps. It is also possible to see that at a specific load, the equivalent stresses and strains of each pattern show clear differences. Hence, this is an indication of that these quantities may be used to evaluate different patterns relatively.

Of the three overlaps tested, 12.5%, 25% and 50%, it is concluded that 12.5% overlap is the best in terms of resisting compressive loads. More generally, both the conducted simulations and physical tests show that less overlap is better from a robustness point of view. The reason for this is likely that the surface taking the load is decreased with increased overlap. However, it still seems like a small overlap is better than no overlap at all. This may be seen both from previous tests conducted at Tetra Pak, and from simulations of the internal pressure of the packages.

The theory that stacking the packages should have no major influence of the response is confirmed by simulations. It is not confirmed by testing, but most likely the strength will decrease with an increase of the number of layers, since the likelihood of including a weaker package is increased.

6.8 Future work

In this thesis, there is a great limitation of the number of packing patterns tested. Hence, in order to get a better foundation, tests of more packing patterns should be conducted. Specifically, it would be interesting to see what effects different longside overlaps would have on the pattern robustness. In continuation to the tests conducted in this thesis, considering that frontside bottom seems to be sensitive, it would also be interesting to put the packages so that only the bottoms were overlapping in order to see if the robustness was increased.

The fracture behaviour of the Tetra Fino® Aseptic package during compression should at this point be quite clear, both from previous results, and from results obtained in this thesis. It would however still be interesting to try to confirm it by conducting e.g. wedge tests of material strips and capture the failure either using tomography or a high speed camera.

The most crucial improvement of the thesis would be to solve the issue of microscopic resolution, i.e. to try to get stresses and strains corresponding better to physical values. This may as mentioned be done by increasing mesh density, but it is not practical at the time being. Another, more reasonable solution would be to model only the seal at a microscopic level and apply an internal pressure. It should be possible to take the pressure from simulations using the presented models, as the macroscopic behaviour is fairly realistic. In a sense, this will be a form of submodeling of the package. Finally, should the fracture behaviour be fully captured computationally, simulations using XFEM should be considered.

Bibliography

[1] Abaqus Manual - SIMULIA User Assistance 2017

[2] Arruda, E. M. and Boyce, M. C. (1993), *"A three-dimensional model for the large stretch behavior of rubber elastic materials"*, J. Mech. Phys. Solids, 41(2), pp. 389-412.

[3] Ottosen N. S. and Petterson N. (1992), *"Introduction to the finite element method"*, Prentice Hall International (UK), Hemel Hempstead

[4] Ristinmaa M. (2016), *"Introduction to non-linear Finite element method"*, Division of Solid Mechanics, Lund University, Lund

[5] Ristinmaa M. and Ottosen N. S. (2005), *"The Mechanics Of Constitutive Modeling"*, Elsevier Ltd., Oxford

[6] Tadmor E., Miller R. and Elliott R. (2011), *Continuum Mechanics and Thermodynamics: From Fundamental Concepts to Governing Equations*, Cambridge University Press, Cambridge

[7] Internal Tetra Pak document. Inclusion of specific information in this thesis has been approved.

[8] www.tetrapak.com/packaging/materials, 2018-03-13

[9] www.tetrapak.com/packaging/tetra-fino-aseptic, 2018-05-07